7-2018

Imaging CF_3I conical intersection and photodissociation dynamics with ultrafast electron diffraction

Jie Yang
SLAC National Accelerator Laboratory, Menlo Park, CA, jieyang@slac.stanford.edu

Xiaolei Zhu
SLAC National Accelerator Laboratory, Menlo Park, CA

Thomas J.A. Wolf
SLAC National Accelerator Laboratory, Menlo Park, CA

Zheng Li
SLAC National Accelerator Laboratory, Menlo Park, CA

J. Pedro F. Nunes
University of York, joao-pedro.figueira-nunes@unl.edu

See next page for additional authors

Authors

Jie Yang, Xiaolei Zhu, Thomas J.A. Wolf, Zheng Li, J. Pedro F. Nunes, Ryan Coffee, James P. Cryan, Markus Gühr, Kareem Hegazy, Tony F. Heinz, Keith Jobe, Renkai Li, Xiaozhe Shen, Theodore Veccione, Stephen Weathersby, Kyle J. Wilkin, Charles Yoneda, Qiang Zheng, Todd J. Martinez, Martin Centurion, and Xijie Wang

Published in *Science* 361 (6 July 2018), pp 64–67.
doi 10.1126/science.aat0049
http://science.sciencemag.org/content/361/6397/64.long

Submitted 14 January 2018; accepted 15 May 2018.

CHEMICAL PHYSICS

Imaging CF_3I conical intersection and photodissociation dynamics with ultrafast electron diffraction

Jie Yang,[1,2]* Xiaolei Zhu,[2,3] Thomas J. A. Wolf,[2]
Zheng Li,[2,4,5] J. Pedro F. Nunes,[6] Ryan Coffee,[2,7,8]
James P. Cryan,[2] Markus Gühr,[2,9] Kareem Hegazy,[2,8]
Tony F. Heinz,[2,10] Keith Jobe,[1] Renkai Li,[1]
Xiaozhe Shen,[1] Theodore Veccione,[1] Stephen Weathersby,[1]
Kyle J. Wilkin,[11] Charles Yoneda,[1] Qiang Zheng,[1]
Todd J. Martinez,[2,3]* Martin Centurion,[11]* and Xijie Wang[1]*

1 SLAC National Accelerator Laboratory, Menlo Park, CA, USA
2 Stanford PULSE Institute, SLAC National Accelerator Laboratory, Menlo Park, CA, USA
3 Department of Chemistry, Stanford University, Stanford, CA, USA
4 Center for Free-Electron Laser Science, Deutsches Elektronen-Synchrotron (DESY), Hamburg, Germany
5 Max Planck Institute for the Structure and Dynamics of Matter, Hamburg, Germany
6 Department of Chemistry, University of York, Heslington, York, UK
7 Linac Coherent Light Source, SLAC National Accelerator Laboratory, Menlo Park, CA, USA
8 Department of Physics, Stanford University, Stanford, CA, USA
9 Institut für Physik und Astronomie, Universität Potsdam, Potsdam, Germany
10 Department of Applied Physics, Stanford University, Stanford, CA, USA
11 Department of Physics and Astronomy, University of Nebraska–Lincoln, Lincoln, NE, USA

* *Corresponding authors email:* jieyang@slac.stanford.edu (J.Y.); todd.martinez@stanford.edu (T.J.M.); martin.centurion@unl.edu (M.C.); wangxj@slac.stanford.edu (X.W.)

Abstract
Conical intersections play a critical role in excited-state dynamics of polyatomic molecules because they govern the reaction pathways of many nonadiabatic processes. However, ultrafast probes have lacked sufficient spatial resolution to image wave-packet trajectories through these intersections directly. Here, we present the simultaneous experimental characterization of one-photon and two-photon excitation channels in isolated CF_3I molecules using ultrafast gas-phase electron diffraction. In the two-photon channel, we have mapped out the real-space trajectories of a coherent nuclear wave packet, which bifurcates onto two potential energy surfaces when passing through a conical intersection. In the one-photon channel, we have resolved excitation of both the umbrella and the breathing vibrational modes in the CF_3 fragment in multiple nuclear dimensions. These findings benchmark and validate ab initio nonadiabatic dynamics calculations.

Light-induced molecular dynamics usually cannot be described within the framework of the Born-Oppenheimer approximation. The picture of nuclear motion on a single adiabatic potential energy surface (PES), determined by treating the fast-moving electrons separately from the slower nuclei, breaks down wherever two or more adiabatic PESs come close in energy (*1*, *2*). At the crossing point of PESs, the degeneracy is lifted along at least two internal degrees of freedom, and the resultant conical intersection guides efficient radiationless transitions between electronic states at specific nuclear configurations (*3*). Examples of important nonadiabatic reactions include photosynthesis (*4*), retinal isomerization in vision (*5*), ultraviolet-induced DNA damage (*6*), and formation of vitamin D (*7*).

Several experimental methods have been developed for studying nonadiabatic dynamics through conical intersections (*8*–*13*). Among these, time-averaged photofragment imaging can identify distinct spectral features of nonadiabatic coupling (*8*, *9*) but does not allow the observation of dynamics in real time. Time-resolved laser spectroscopy is the most widely used real-time method for following electronic dynamics, but nuclear dynamics can only be inferred on the basis of an indirect comparison with simulated transient spectroscopic features (*11*–*14*). In addition, comparison with theoretical predictions requires explicit modeling of the probing process, which can be more complex than the nonadiabatic dynamics in question. Recent developments in both x-ray (*15*, *16*) and electron-based (*17*, *18*) time-resolved diffraction techniques open an opportunity for direct imaging of conformational changes during chemical reactions—molecular movies with atomic resolution in space and time. Despite the great importance of nonadiabatic dynamics through conical intersections, spatiotemporal resolution has not been sufficient to image a coherent nuclear wave packet traversing a conical intersection with time-resolved diffraction techniques.

The nonadiabatic transitions of molecules between different PESs are inherently quantum mechanical. A wide variety of computational methods can be used to simulate dynamics through conical intersections. For small systems, nonadiabatic dynamics can be treated with exact full quantum dynamics (*19*) and the highly accurate multiconfigurational time-dependent Hartree approximation (*20*). For larger systems, semiclassically motivated approaches such as Tully's surface hopping (*21*), Meyer-Miller formalism (*22*), or ab initio multiple spawning (AIMS) (*23*) are routinely used. Although simulations can provide rich details of the dynamics through conical intersections, nontrivial approximations at many different stages of the calculations are required, even for relatively small systems. Therefore, confirmation with experimental measurements is crucial.

Here, we report the direct imaging of both conical intersection dynamics and photodissociation dynamics of gas-phase CF_3I molecules with atomic resolution by use of ultrafast gas-phase electron diffraction (UGED). A 264.5-nm pump laser pulse initiates two photoexcitation channels: a one-photon transition to the dissociative A band and a two-photon transition to the [$5p\pi^3$, $^2\Pi_{1/2}$](7s) (*24*) Rydberg state (referred to as 7s below) (*25*), as illustrated in **Fig. 1**. The adiabatic dissociation dynamics through A-band excitation of

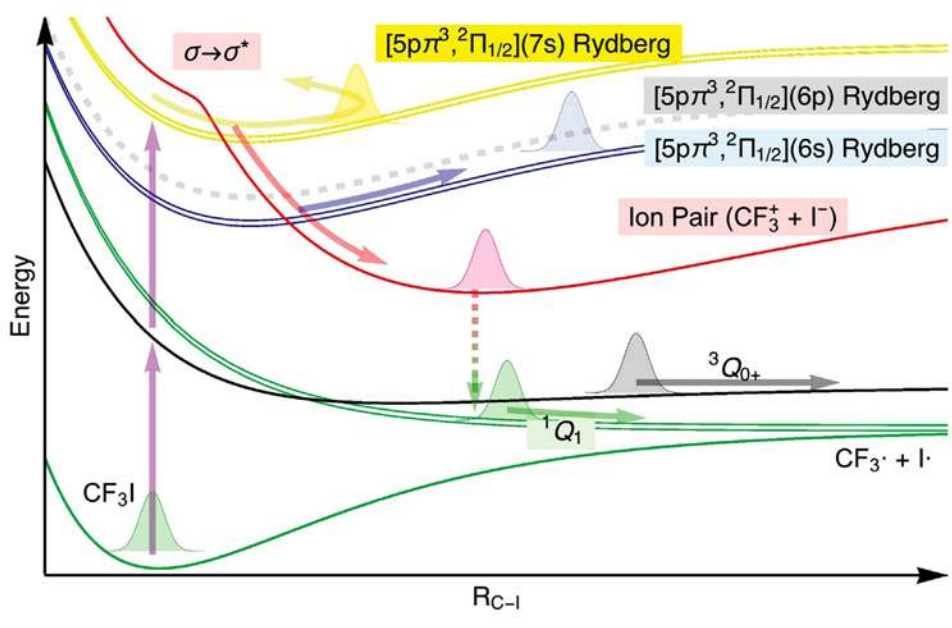

Fig. 1. Two-channel excitation in CF_3I. PES along the C–I bond length coordinate, with major states labeled and reaction pathways marked by arrows. Color coding indicates different electronic states: yellow, 7s; red, ion pair (IP); blue, 6s; green, valence open-shell states. C_{3v} symmetry is retained in this plot. The two relevant states in the A band are $^3Q_{0+}$ and $^1Q_1$ (using Mulliken notation). The 6s, 7s, and $^1Q_1$ states are of E symmetry, as indicated by two closely spaced parallel surfaces.

CF_3I and its analog, CH_3I, have been studied extensively (*26–29*). We created a multidimensional movie of the structural changes in the CF_3 fragment immediately after iodide dissociation, with a precision of ±0.01 Å in bond length and ±1° in bond angle. Various groups have studied the two-photon transition into the 7s channel by using pump-probe photoelectron and photoion spectroscopy (*25, 30–32*). These studies identified the decay time scale and anisotropy of fragment ions, but the reaction pathway remained elusive. Specifically, it was only a speculation that a nearby ion-pair state might be involved in the reaction dynamics (*31*). We have mapped out the nuclear wave-packet trajectory in real space, which directly shows wave-packet bifurcation though a conical intersection. Through cross-verification with AIMS simulations, we have clarified that the ss* state correlates asymptotically to a CF_3^+–I^- ion-pair state (referred to as IP) at large C–I separation, and that this state plays a key role in this channel. The reaction pathway is predominantly determined by the nonadiabatic coupling between IP and multiple states: the 7s and [5pπ^3, $^2\Pi_{1/2}$](6s) Rydberg states (referred to as 6s below) and valence states.

The UGED experimental setup is shown in **Fig. 2**A, which is described in detail in (*33*, *34*) and the supplementary materials. For diffraction pattern

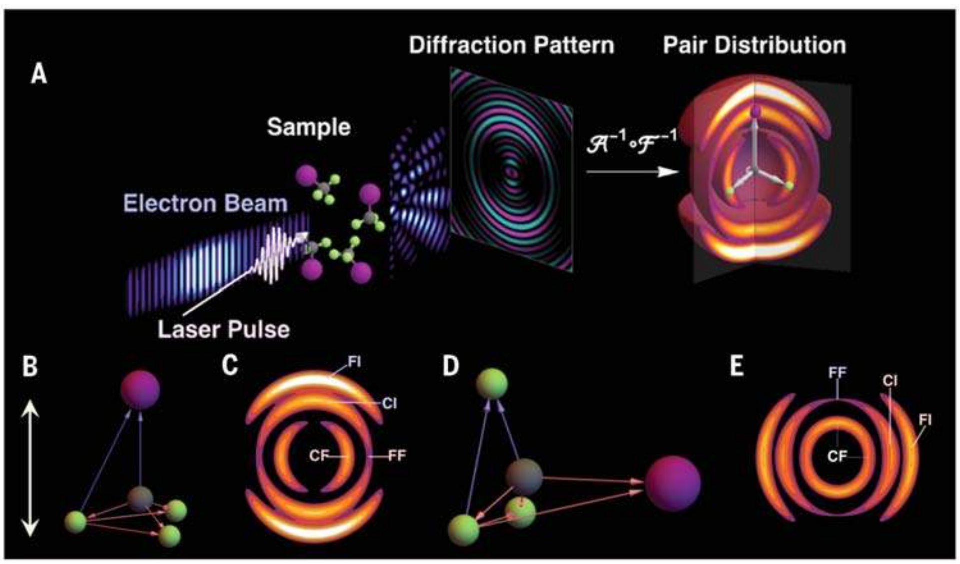

Fig. 2. Real-space analysis of diffraction patterns. (A) Schematic drawing of the experiment. **(B)** A model for a CF_3I molecule oriented along the laser polarization axis. **(C)** Simulated PDF for molecular ensemble with a $\cos^2\theta$ angular distribution. **(D)** A model for a CF_3I molecule oriented perpendicular to the laser polarization. **(E)** Simulated PDF for molecular ensemble with a $\sin^4\theta$ angular distribution. In (B) to (E), the laser polarization is indicated by the double-headed arrow. Gray, light green, and purple represent carbon, fluorine, and iodine, respectively.

analysis, we used a two-dimensional (2D) Fourier transform followed by Abel inversion to convert data from momentum space to real space. This procedure returns a pair-distribution-function (PDF) that reports all the interatomic distances, as explained in Fig. 2, B to E.

The one-photon channel preferentially excites molecules with the C–I axis aligned along the laser polarization. This results in a $\cos^2\theta$ angular distribution of excited-state molecules, where θ is the angle between the C–I bond and the laser polarization(Fig. 2, B & C). In this case, C–I and F–I pairs mostly appear in the parallel direction ($PDF_{||}$), and the C–F and F–F pairs preferentially appear in the perpendicular direction ($PDF_{\perp}$). The two-photon channel corresponds to a perpendicular excitation ($\sin^4\theta$ distribution) (Fig. 2, D and E). In this case, C–I and F–I pairs preferentially appear in $PDF_{\perp}$, whereas C–F and F–F slightly favor $PDF_{||}$. This analysis simultaneously yields information about atom pair distances and their corresponding angular distribution, which is critical for assigning the reaction channels and acquiring multidimensional structural reconstructions of the target molecule during the reaction.

We first concentrated on the experimental evidence for nonadiabatic dynamics in the two-photon channel. The experimental $\Delta PDF_{\perp}$ as a function of pump-probe time delay is shown in **Fig. 3**A, with blue indicating loss and red indicating gain of atom pair distances as compared with unexcited molecules. This signal contains structural information from both two-photon (C–I and F–I pairs) and one-photon (C–F and F–F pairs) channels. They can be roughly separated by time scales: The one-photon channel dominates the signal at time delay (Δt) < 200 fs, and the two-photon channel dominates the signal at Δt > 200 fs, at which point the only contribution from the one-photon channel, once dissociation is complete, is a smoothly decaying signal due to rotational dephasing (supplementary materials). The evolution of $\Delta PDF_{\perp}$ is plotted in Fig. 3B at three specific pair distances: the initial C–I distance (2.14 Å), a position between the initial C–I and F–I distances (2.52 Å), and the initial F–I distance (2.90 Å). After a time delay of Δt = 100 fs, the signals corresponding to 2.14 and 2.52 Å oscillate out of phase. This result clearly indicates that the C–I bond is vibrationally excited, and the ~200-fs period matches well with the documented C–I stretching mode on the 7s surface (*35*). The 2.9-Å signal shows oscillatory decay up to Δt = 400 fs, with a surprisingly strong recurrence at Δt = 500 fs. This recurrence time scale cannot be explained by any previously reported vibrational mode on the 7s surface.

The real-space reaction trajectory is encoded in $\Delta PDF_{\perp}$ and can be extracted by using a ridge-detection algorithm. First, we extracted the two-photon $PDF_{\perp}$ by removing a common decaying signal from $\Delta PDF_{\perp}$. Second, we used a ridge-detection algorithm to locate 1D local maxima, or ridges. Last, we generated the reaction trajectory by connecting nearby ridges

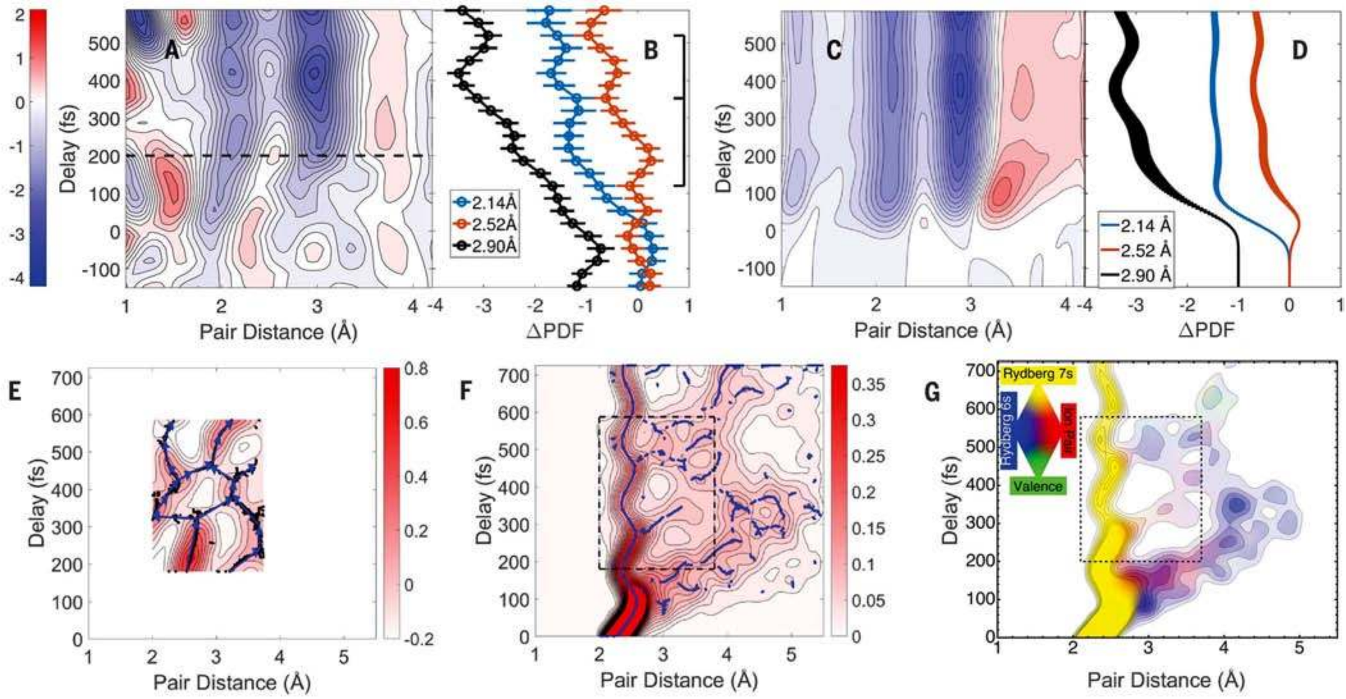

Fig. 3. Nuclear wave-packet conical intersection dynamics in the two-photon channel. (A) Experimental $\Delta PDF_{\perp}$, smoothed by an 80-fs Gaussian kernel. The dashed line at 200 fs shows a rough separation between contributions from the one-photon and the two-photon channels. **(B)** Experimental time evolution of $\Delta PDF_{\perp}$ at 2.14, 2.52, and 2.90 Å, error bars corresponding to 1 SD of a bootstrapped dataset (supplementary materials). A comb illustrates the first two periods of the C–I stretching vibration. **(C)** Simulated $\Delta PDF_{\perp}$ of the two-photon channel. **(D)** Simulated time evolution of $\Delta PDF_{\perp}$ at 2.14, 2.52, and 2.90 Å. Curve width represents 1 SD of a bootstrapped simulation dataset. **(E)** Two-photon $PDF_{\perp}$ generated by removing a common decaying signal from $\Delta PDF_{\perp}$. Black dots indicate identified ridges, and blue arrows indicate trajectories generated by connecting nearby ridges. The axes are the same as (F) for easy comparison. **(F)** Simulated nuclear wave packet along the C–I coordinate. Blue dots indicate identified ridges. **(G)** Simulated nuclear wave packet along the C–I coordinate as in (F), with color-coding to reflect diabatic state character, as shown in the legend. The dashed box in (F) and (G) matches the region captured in (E). The simulation results are generated by averaging over more than 2000 spawned trajectories from 50 initial conditions. In (B) and (D), the 2.90 Å curve is shifted by −1 for visibility.

(supplementary materials). The excited-state $PDF_{\perp}$ is shown in Fig. 3E together with identified ridges (Fig. 3E, black dots) and trajectory (Fig. 3E, blue arrows). In this trajectory map, at least two wave-packet bifurcation events can be identified: One occurs at ~2.7 Å/300 fs, and the other at ~2.4 Å/420 fs. In addition, a two-branch crossover event can be seen at ~3.3 Å/400 fs. These features serve as strong evidence for the involvement of multiple electronic states and nonadiabatic coupling through conical intersections.

We support our experimental results by using AIMS simulations. The nuclear wave-packet density is shown in Fig. 3G projected along the C–I distance and color-coded according to diabatic state character. The color mixing reflects the composition of the population on these diabatic states. For example, orange indicates that 7s and IP states are dominantly populated, and magenta indicates a dominant population in 6s and IP. Upon excitation, the wave packet takes ~100 fs to reach the 7s-IP conical intersection seam, where electronic transitions cause the wave packet to bifurcate into two branches. The branch remaining on the 7s surface has a strong C–I stretching character; the center of the wave packet oscillates with a period of about 200 fs, with relatively little dispersion. For the branch transferred to IP, a large fraction of the wave-packet amplitude is further transferred to the 6s surface through the IP-6s conical intersection seam and returns to the Franck-Condon region at ~500 fs. The vibrational wave packet on 7s reaches the 7s-IP conical intersection seam again at ~280 and 480 fs, giving rise to the second and the third population transfer events to the 6s surface through IP. The third outgoing wave packet on IP transiently overlaps with the returning wave packet on 6s, causing a strong recurrence of population at 500 fs at ~3Å.

The simulated $\Delta PDF_{\perp}$ of the two-photon channel is shown in Fig. 3C, and its evolution at 2.14, 2.52, and 2.90 Å is shown in Fig. 3D. Comparison between Fig. 3, A and C, and Fig. 3, B and D, shows that the ~200-fs vibration and the strong recurrence at 2.90 Å/500 fs match very well. The vibration is more pronounced in the experimental data, possibly because of various approximations adopted in the simulation. The result of the ridge-detection algorithm on the simulated nuclear wave packet is shown in Fig. 3F. The dashed box in Fig. 3F shows a very similar trajectory as that in Fig. 3E: Two wave-packet bifurcation events can be found at 2.6 Å/270 fs and 2.5 Å/460 fs, and a two-branch crossover event is seen at ~3.6 Å/420 fs. All three events are within a 0.3-Å/40-fs spatiotemporal displacement in comparison with experimental data. Comparison between Fig. 3E and Fig. 3F shows that the real-space reaction trajectory, including nonadiabatic events through conical intersections, is directly captured in the experimental data.

We next concentrated on photodissociation after single-photon excitation to the $^3Q_0$ state and explored the ensuing structural changes in multiple nuclear coordinates. After the breaking of the C–I bond, the most obvious diffraction signature is the loss of C–I and F–I atom pairs. This is reflected

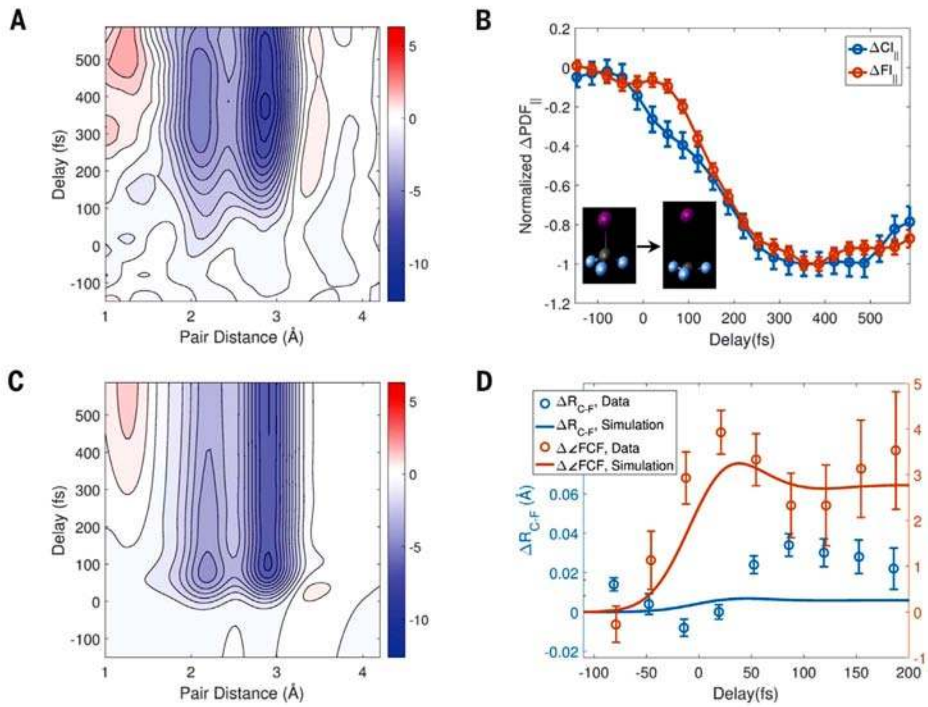

Fig. 4. Multidimensional structural evolution during photodissociation in the one-photon excitation channel. (A) Experimental $\Delta PDF_{||}$, smoothed by an 80-fs Gaussian kernel. **(B)** C–I and F–I bleaching signal in $\Delta PDF_{||}$. Different onset time reflects the transient recoil of the carbon atom, as shown in the inset. Error bars correspond to 1 SD of a bootstrapped dataset. **(C)** Simulated $\Delta PDF_{||}$ of the one-photon channel. **(D)** Structural evolution of CF_3 group from experiment (circles with error bars representing the standard error of the fit), plotted together with temporal-blurred structural evolution from AIMS simulation (solid curves). R_{C-F} and ∠FCF are color-coded blue and red, respectively. In (D), the vertical axis ranges for length and angle are adjusted to match each other with a 1.33-Å (ground state C–F distance) radius.

by the two strong bleaching bands in $\Delta PDF_{||}$ around 2.14 and 2.9 Å in **Fig. 4**A. The time dependence of these two bleaching signals is plotted in Fig. 4B. The C–I bleaching signal starts ~30 fs earlier than the F–I signal on account of comparatively fast recoil of the lighter carbon relative to the heavier iodine. Both the iodine and the three fluorine atoms move on a slower time scale, leading to an observable delay between the loss of C–I pair and F–I pair. The AIMS simulation shows a 16-fs separation of the two bleaching signals, which is in reasonable agreement with the experiment. The simulated $\Delta PDF_{||}$ of the one-photon channel is given in Fig. 4C. Three main features in Fig. 4A are reproduced in Fig. 4C: The two bleaching bands correspond to the loss of C–I and F–I atom pairs, and a positive feature ~1.3 Å after 300 fs is caused by the rotational dephasing of CF_3 radicals.

More details about the very early motion after photodissociation can be extracted from the C–F and F–F pairs encoded in $\Delta PDF_{\perp}$ for $\Delta t < 200$ fs. We performed a χ^2fit in $\Delta PDF_{\perp}$ in order to extract the change of molecular structure (supplementary materials) and the fitted C–F bond length change (ΔR_{C-F}) and F–C–F bond angle change (Δ∠FCF) are given in Fig. 4D. The dynamics assembled from the data are shown in movie S1. Upon dissociation, the ∠FCF immediately opens up by ~4°, followed by R_{C-F} elongating by ~0.03 Å with a ~50-fs delay.

We performed AIMS simulations on the $^3Q_0$ state. Upon dissociation, both the umbrella and the breathing vibrational modes are strongly activated with a difference in phase. The angle ∠FCF immediately opens up and vibrates, whereas R_{C-F} shrinks slightly before the strong lengthening. This difference in initial motion is again caused by the recoil of the carbon atom, and when blurred by the instrumental response, results in a measurable delay between the opening of ∠FCF and stretching of R_{C-F}. The red and blue lines in Fig. 4D indicate the simulated changes in R_{C-F} and ∠FCF convolved with an 80-fs Gaussian cross-correlation function so as to incorporate instrumental response. The simulation predicts umbrella opening, R_{C-F} lengthening, and the delay between these, which is in agreement with the experimental observation. A small amount (10%) of intersystem crossing from the $^3Q_0$ to the $^1Q_1$ state has been reported in previous experiments (*27*), but this effect is not observable in our experiments owing to the spatiotemporal resolution limit.

We have shown that UGED can track a nuclear wave packet with atomic spatiotemporal resolution during nonadiabatic processes involving conical intersections, measuring multidimensional nuclear geometry changes, and simultaneously observing dynamics from different excitation channels in polyatomic molecules. In addition, UGED provides a direct probing method for nuclear degrees of freedom, complementing the standard ultrafast laser spectroscopic techniques that directly probe electronic degrees of freedom. Both the experiment and the data analysis of UGED are generally applicable to a wide range of systems in the gas phase. This approach opens the door for studying many important problems in fundamental photochemistry.

References & Note

1. G. Herzberg, *Molecular Spectra and Molecular Structure III (Polyatomic Molecules)* (1966).
2. J. Michl, V. Bonacic-Koutecky, *Electronic Aspects of Organic Photochemistry* (Wiley, 1990).
3. W. Domcke, D. R. Yarkony, H. Köppel, *Conical Intersections—Electronic Structure, Dynamics and Spectroscopy* (World Scientific Pub, 2004).
4. Y.-C. Cheng, G. R. Fleming, *Annu. Rev. Phys. Chem.* 60, 241–262 (2009).
5. D. Polli *et al.*, *Nature* 467, 440–443 (2010).

6. C. E. Crespo-Hernández, B. Cohen, P. M. Hare, B. Kohler, *Chem. Rev.* 104, 1977–2019 (2004).
7. M. F. Holick, *Fed. Proc.* 46, 1876–1882 (1987).
8. J. S. Lim, S. K. Kim, *Nat. Chem.* 2, 627–632 (2010).
9. J. A. DeVine *et al.*, *Science* 358, 336–339 (2017).
10. H. J. Wörner *et al.*, *Science* 334, 208–212 (2011).
11. A. Stolow, A. E. Bragg, D. M. Neumark, *Chem. Rev.* 104, 1719–1757 (2004).
12. J. Brazard, L. A. Bizimana, T. Gellen, W. P. Carbery, D. B. Turner, *J. Phys. Chem. Lett.* 7, 14–19 (2016).
13. T. J. A. Wolf *et al.*, *Nat. Commun.* 8, 29 (2017).
14. A. H. Zewail, *Angew. Chem. Int. Ed.* 39, 2586–2631 (2000).
15. M. P. Minitti *et al.*, *Phys. Rev. Lett.* 114, 255501 (2015).
16. J. Küpper *et al.*, *Phys. Rev. Lett.* 112, 083002 (2014).
17. J. Yang *et al.*, *Phys. Rev. Lett.* 117, 153002 (2016).
18. A. A. Ischenko, P. M. Weber, R. J. D. Miller, *Chem. Rev.* 117, 11066–11124 (2017).
19. R. Chen, H. Guo, *J. Chem. Phys.* 105, 3569–3578 (1996).
20. H.-D. Meyer, U. Manthe, L. S. Cederbaum, *Chem. Phys. Lett.* 165, 73–78 (1990).
21. J. C. Tully, *J. Chem. Phys.* 93, 1061–1071 (1990).
22. H.-D. Meyer, W. H. Miller, *J. Chem. Phys.* 70, 3214–3223 (1979).
23. M. Ben-Nun, J. Quenneville, T. J. Martínez, *J. Phys. Chem. A* 104, 5161–5175 (2000).
24. The square bracket encloses the electronic configuration, symmetry, and spin-orbit state of the cation core, and the parenthesis indicates the configuration of the Rydberg electron.
25. S. Yin *et al.*, *Chem. Phys. Lett.* 372, 904–910 (2003).
26. L. J. Butler, *Annu. Rev. Phys. Chem.* 49, 125–171 (1998).
27. F. Aguirre, S. T. Pratt, *J. Chem. Phys.* 122, 234303 (2005).
28. M. Zahedi, J. Harrison, J. W. Nibler, *J. Chem. Phys.* 100, 4043–4055 (1994).
29. A. Furlan, T. Gejo, J. R. Huber, *J. Phys. Chem.* 100, 7956–7961 (1996).
30. H. P. Liu, Z. G. Sun, S. D. Hogan, N. Q. Lou, *Eur. Phys. J. D* 40, 357–362 (2006).
31. W. G. Roeterdink, M. H. M. Janssen, *Phys. Chem. Chem. Phys.* 4, 601–612 (2002).
32. W. G. Roeterdink, M. H. M. Janssen, *Chem. Phys. Lett.* 345, 72–80 (2001).
33. J. Yang *et al.*, *Nat. Commun.* 7, 11232 (2016).
34. S. P. Weathersby *et al.*, *Rev. Sci. Instrum.* 86, 073702 (2015).
35. S. Eden, P. Limão-Vieira, S. V. Hoffmann, N. J. Mason, *Chem. Phys.* 323, 313–333 (2006).
36. J. Yang *et al.*, Imaging CF3I conical intersection and photodissociation dynamics by ultrafast electron diffraction. Figshare (2018); doi:10.6084/m9.figshare.6169427.

Acknowledgments — We thank G. M. Stewart from SLAC National Accelerator Laboratory for the assistance with making movie S1.

Funding: The experimental part of this research was performed at SLAC MeV-UED, which is supported in part by the U.S. Department of Energy (DOE) Office of Basic Energy Sciences (BES) SUF Division Accelerator and Detector R&D program, the LCLS Facility, and SLAC under contracts DE-AC02-05-CH11231 and DE-AC02-76SF00515. J.Y., T.F.H., J.P.C., R.C., T.J.A.W., X.Z., and T.J.M. acknowledge support by the AMOS program within the Chemical Sciences, Geosciences, and Biosciences Division, BES of the DOE under contract DE-AC02-76SF00515. J.P.F.N. acknowledges support by the Wild Overseas Scholars Fund of Department of Chemistry, University of York. T.J.M. acknowledges support from Office of Naval Research grant N00014-12-1-0828 and the Global Climate and Energy Project. This work used the XStream computational resources supported by the National Science Foundation Major Research Instrumentation program (ACI-1429830). Z.L. acknowledges support by the Volkswagen Foundation. M.G. is funded via a Lichtenberg Professorship of the Volkswagen Foundation. K.J.W. and M.C. were supported by the DOE Office of Science, BES under award DE-SC0014170.

Author contributions: J.Y., T.J.A.W., J.P.F.N., J.P.C., K.H., R.L., X.S., T.V., S.W., Q.Z., and X.W. carried out the experiments; R.C., J.P.C., J.Y., T.J.A.W, and S.W. developed the laser system; M.G., J.Y., K.J., C.Y., X.S., R.L., and K.J.W. constructed and commissioned the setup for gas phase experiments; J.Y. performed the data analysis with input from M.C., T.J.A.W, J.P.C, X.Z., T.F.H., and M.G; M.C., J.Y., M.G., X.Z., and Z.L. conceived the experiment; X.Z. and T.J.M. performed the AIMS simulations; Z.L. and T.J.M performed the 3D full quantum wave-packet simulation; and J.Y., X.Z., T.J.M, M.G., M.C., and X.W. prepared the manuscript with discussion and improvements from all authors.

Competing interests: The authors declare no competing interests.

Data and materials availability: Both the experimental data and the simulated trajectories, after basic noise removal and statistical averaging, are available on figshare.com (*36*). The raw experimental data are archived at SLAC's centrally managed GPFS storage, and the raw simulated data are stored at T.J.M.'s group at Stanford University. All the raw data will be made available upon request.

Supplementary Materials follow.

(Also online at www.sciencemag.org/content/361/6397/64/suppl/DC1)

Materials and Methods
Supplementary Text
Figs. S1 to S17
Table S1
References (*37–63*)

Movie S1 is attached and downloadable from the archive cover page for this paper. This movie shows the structural response of CF3 group during dissociation, and is made with data shown in Table S1, or Fig. 4D in the main text. The motion is presented in the rest frame of the carbon atom. The left-hand side gives a ball-and-stick model of the molecule, and the righthand side shows a zoom-in view of the trajectory of one of the fluorine atoms. C-F bond length and F-C-F bond angle are displayed in the bottom right.

www.sciencemag.org/content/361/6397/64/suppl/DC1

Supplementary Material for

Imaging CF_3I conical intersection and photodissociation dynamics with ultrafast electron diffraction

Jie Yang*, Xiaolei Zhu, Thomas J. A. Wolf, Zheng Li, J. Pedro F. Nunes, Ryan Coffee, James P. Cryan, Markus Gühr, Kareem Hegazy, Tony F. Heinz, Keith Jobe, Renkai Li, Xiaozhe Shen, Theodore Veccione, Stephen Weathersby, Kyle J. Wilkin, Charles Yoneda, Qiang Zheng, Todd J. Martinez*, Martin Centurion*, Xijie Wang*

*Corresponding author. Email: jieyang@slac.stanford.edu (J.Y.); todd.martinez@stanford.edu (T.J.M.); martin.centurion@unl.edu (M.C.); wangxj@slac.stanford.edu (X.W.)

Published 6 July 2018, *Science* **361**, 64 (2017)
DOI: 10.1126/science.aat0049

This PDF file includes:

Materials and Methods
Supplementary Text
Figs. S1 to S17
Table S1
References

Other Supplementary Material for this manuscript includes the following:
(available at www.sciencemag.org/content/361/6397/64/suppl/DC1)

Movie S1

Materials and Methods

Experimental Methods

The MeV UGED setup at SLAC has been described in detail previously (*33*, *34*). Briefly, the radio-frequency (rf) gun, powered by an S-band klystron, provides 80 MV/m accelerating field. The typical amplitude and phase root-mean-square (rms) stability of the rf amplitude and phase are 2.5×10^{-4} and 30fs, respectively. Electron beam energy can be tuned continuously up to ~5 MeV. In this experiment, the kinetic energy is set at 3.7 MeV, each electron pulse contains roughly 10^4 electrons and is focused to a diameter of 200 µm FWHM.

A linearly polarized 200 µJ pump laser pulse with wavelength centered at 264.5 nm with a 1.3 nm FWHM bandwidth is focused to a 250 µm diameter spot, giving a fluence of 400 mJ/cm^2. The duration of the pump UV pulse is estimated to be 80fs FWHM.

The sample (Trifluoroiodomethane, 99.9%) was purchased from Alfa Aesar without further purification. CF_3I gas is introduced into the vacuum chamber with a pulsed 100 µm nozzle, with the backing pressure set to 1 bar. The nozzle is heated to 150 °C to avoid clustering of the target molecules.

The electron and laser beam are co-propagating with a 5-degree angle, intersecting the gas jet at roughly 250 µm underneath the nozzle exit. The overall instrumental response is estimated to be around 150 fs FWHM. The gas jet size is around 300 µm FWHM with a number density on the order of 10^{16} cm^{-3} at the interaction region. The system is operated at a repetition rate of 120 Hz. Spatial and temporal overlap between the pump laser and probe electron beam is achieved by plasma-induced lensing effect(*37*). Diffraction patterns at each time delay are accumulated for 100 minutes.

The electron detector is comprised of a P43 phosphor screen with a center hole, a 45° mirror with a center hole, an imaging lens and an electron-multiplying charge-coupled device. Each frame is integrated for 20 seconds before read-out.

The excitation percentage of the one-photon channel is estimated to be 5.6% using $\Delta PDF_{\parallel}$, the branching ratio of the one-photon and two-photon process is estimated to be between 85:15 and 75:25.

We have performed a power scan and confirmed that the dissociation signal remains in the linear regime at this pump condition. Fig. S1 plots the strongest feature of C-I bond dissociation in the diffraction pattern—an increase of diffraction signal between 1.6 and 2.3 Å^{-1}–as a function of pump pulse energy. This power scan shows that the dissociation signal is linear with pump energy at 200 µJ pump pulse energy.

Diffraction Pattern Analysis

In time-resolved diffraction experiments, photoselection rules generate anisotropy in diffraction patterns, which contain information about both the 3-D molecular structure and the angular distribution of the molecule(*38*).

In electron diffraction, each nucleus and its surrounding electrons scatter the incident electrons Coulombically, and the scattered spherical waves interfere on the detector generating a diffraction pattern. In this process, each atom pair gives rise to a sinusoidal signal, and the single-molecule diffraction pattern of an N-atom molecule at a specific time t and a specific orientation $\vec{a}$ can be written as (*38*),

$$I^{\vec{a}}(t;\vec{s}) = \sum_{i=1}^{N}\sum_{l=1}^{N} f_i(s) f_l(s) e^{i(\vec{s}\cdot\vec{r}_{il}(\vec{a};t))} \tag{1}$$

where the vector $\vec{a}$ represents the molecular orientation, f_i is the complex scattering amplitude of atom i, $\vec{s}$ is the momentum transfer vector and $\vec{r}_{il}(\vec{a};t)$ is the vector pointing from atom i to atom l at a specific time t. For an ensemble of molecules, the total diffraction pattern is simply an incoherent sum of all the single-molecule diffraction patterns,

$$I(t;\vec{s}) = \sum_{\vec{a}} I^{\vec{a}}(t;\vec{s}) \tag{2}$$

Equation (1) and (2) show that at each specific time t, the diffraction pattern in 3-D momentum space $I(t;\vec{s})$ is the sum of the Fourier transform of atom pairs, and the 3-D inverse Fourier transform of $I(t;\vec{s})$ gives the ensemble of atom pairs in real-space. Here we measure only a 2-D area in momentum space $I(s_x, s_y, s_z{\approx}0)$, where z is the direction of electron propagation. The 3.7 MeV electron beam has very short wavelength of 0.3 pm, which corresponds to an extremely flat Ewald sphere, so $s_z=0$ is a good approximation. The 2-D inverse Fourier transform of the diffraction pattern $I(s_x, s_y, s_z=0)$ gives the Abel transform (z-integral) of the atom pair ensemble.

$$\begin{aligned} \mathbb{F}_{2D}^{-1}[I(t;s_x,s_y)] &= \iint I(t;s_x,s_y) e^{-i(s_x x + s_y y)} ds_x ds_y \\ &= \int_{-\infty}^{+\infty} \sum_{\vec{a}} \sum_{i=1}^{N}\sum_{l=1}^{N} F_i F_l \otimes \delta(\vec{r} - \vec{r}_{il}(\vec{a};t)) dz \end{aligned} \tag{3}$$

where F_i is the 2D Fourier transform of f_i, the symbol $\otimes$ represents a convolution and $\delta(\vec{r})$ is the Dirac delta function.

An Abel inversion of equation (3) gives:

$$A^{-1}\{\mathbb{F}_{2D}^{-1}[I(t;s_x,s_y)]\} = \sum_{\vec{a}} \sum_{i=1}^{N}\sum_{l=1}^{N} F_i F_l \otimes \delta(\vec{r} - \vec{r}_{il}(\vec{a};t)) \tag{4}$$

Eq. (4) shows that a 2D Fourier transform followed by a z-direction Abel inversion yields a sum of all the atom pairs in real space.

This diffraction pattern analysis practice is explained graphically in Fig. S2A-D. Fig. S2A shows the simulated diffraction pattern of the ground state CF_3I assuming a $\cos^2\theta$ angular distribution, where θ is the angle between the laser polarization and the C-I bond of the molecule. Fig. S2B gives its 2-D fast Fourier transform (FFT), which yields a *z*-projection of the pair distribution function (PDF), as shown in Eq. (3). Fig. S2C shows the PDF after Abel inversion with the pBasex algorithm(*39*), in which the blurring due to *z*- projection is removed. Fig. S2D represents the PDF in polar coordinates, where both the distance and the angular distribution of each atom pair can be clearly identified. We split the angular-resolved PDF into 9 sections, with each section covering a 10° angular range. The two important sections— $PDF_{\parallel}$ (0°-10°) and $PDF_{\perp}$ (80°-90°) are shown by the colored strips in Fig. S2D. Four atom pairs are present in ground state CF_3I: C-F pair at 1.33Å, C-I pair at 2.14Å, F-F pair at 2.15Å, and F-I pair at 2.89Å. Their angle to the C_3 molecular symmetry axis are 69°, 0°, 90° and 21°, respectively. Therefore, for a parallel excitation, C-I and F-I will appear mostly in $PDF_{\parallel}$ while C-F and F-F will appear mostly in $PDF_{\perp}$. For a perpendicular excitation, C-I and F-I will appear mostly in $PDF_{\perp}$ while C-F and F-F will appear slightly preferentially in $PDF_{\parallel}$, as shown in Fig. 2B-E in the main text.

In our experimental data, a few additional filters are applied to suppress noise, including Legendre filtering(*40*), a low pass filter in momentum space ($e^{-s^2/7^2}$) and a temporal Gaussian filter (80fs FWHM). In the 2D FFT, momentum transfer up to s=9.5Å^{-1} is used, and a zero-padding technique is applied. The low s (s<1.2Å^{-1}) signal is unavailable in the experiment due to a center hole in the phosphor screen that transmits the unscattered electron beam. We fit the region 1.2Å^{-1}<s<3.4Å^{-1} to the simplest dissociation model—instantaneous loss of C-I and F-I atom pairs and use the low s from this model to fill in the missing region. We tested the effect of this fitting using simulated diffraction patterns. It significantly reduces the signal strength of the fast-moving dissociation wavepacket, but otherwise has minimum effect on the signal between 1 and 4 Å.

A bootstrapping method is used to calculate the statistical uncertainty. At each time delay, 300 diffraction patterns are measured in the experiment. This dataset is re-sampled 100 times, 300 patterns each time, using a standard bootstrapping method. This process generates 100 bootstrapped diffraction patterns. Each bootstrapped diffraction pattern is analyzed using the full data analysis routine described above, and the standard deviation of the 100 results is taken as the standard error.

The AIMS simulation gives time-dependent nuclear wavefunctions, expressed as a superposition of frozen Gaussian basis functions that evolve along classical trajectories (also known as trajectory basis functions or TBFs). The initial positions and momenta for these TBFs are sampled from a harmonic Wigner distribution at 0K around the global minimum energy geometry on the ground state, aligned so that the C_{3v} rotational axis is parallel to the z-axis. The transition dipole moments remain nearly perpendicular to the molecular axis within the Wigner distribution (Fig. S3). The mean angle between the CI axis and the transition dipole from ground to 7s Rydberg state is 90.0° and the standard deviation is smaller than 2°. This result confirms that the excitation process can be treated under C_{3v} point group symmetry. To simulate the PDF from AIMS trajectories, we need to take into account the proper angular distribution generated by the photoselection rules. For each spawned trajectory, we simulate an ensemble diffraction pattern by applying an angular distribution to all three Euler angles (θ, φ, χ). Here we follow the convention given by Zare (*41*), where θ is the initial polar angle (the angle between C-I bond and the laser polarization at time zero), φ is the initial azimuthal angle in the lab frame and χ is the initial azimuthal angle in the molecular frame. The angles φ and χ are always sampled uniformly, and θ is sampled as $\cos^2\theta$ for the one-photon channel and as $\sin^4\theta$ for the two-photon channel, according to the photoselection rules. Once the ensemble diffraction pattern is simulated, the same diffraction pattern processing routine applied to the experimental data is applied to the simulated diffraction patterns to generate $\Delta PDF_{\parallel}$ and $\Delta PDF_{\perp}$.

Validity of the Fourier Analysis

In the Fourier transform, the available *s* region is cropped between 1.2 and 9.5 $Å^{-1}$. In order to justify the validity of the Fourier analysis routine and to explore the consequences of the limited *s* range, we calculated a real-space $\Delta PDF_{\perp}$ from simulated trajectories in three separate ways:

A. Simulate diffraction patterns with *s* range from 0 to 12.5 $Å^{-1}$ and process the simulated diffraction pattern in the same way the experimental data was processed.
B. Simulate diffraction pattern, crop the *s* range to match the experimental range (from 1.2 to 9.5 $Å^{-1}$), and go through all the same data processing routines as the experimental data.
C. Directly convert the simulated trajectory to $\Delta PDF_{\perp}$ using Eq. (4). Only C-I and F-I atom pairs are considered because of the photoselection rule.

The results are shown in Fig. S4A-C. The three simulation methods show very similar features, both the C-I stretching motion and the revival at 500fs can be identified. This result demonstrates that the missing *s* range and the filtering in the Fourier analysis does not alter the main feature of the data.

Ridge Detection for Mapping Wavepacket Trajectory

In Fig. 3E and Fig. 3F in the main text, a ridge detection algorithm is used to retrieve wavepacket trajectories from the two-photon $PDF_{\perp}$. Here we explain the details of this process.

The direct experimental measurement is $\Delta PDF_{\perp}$, which has three components: #1) $\Delta PDF_{\perp}$ from the two-photon channel that includes all the non-adiabatic dynamics; #2) $\Delta PDF_{\perp}$ from the one-photon channel that include a monotonic decaying signal due to rotational dephasing; and #3) $\Delta PDF_{\perp}$ from the ground state that does not change with time. Ridges in #1 give the wavepacket trajectory of interest, but the strong bleaching bands in #2 and #3 will shift the location of the local maxima. We try to isolate #1 from #2 and #3 by adding back the trivial bleaching signal. First, we estimate the shape of the bleaching signal by taking the average over all points after Δt=200 fs. Secondly, for each time delay we calculate the amplitude of the bleaching signal using a least-square solver for linear equations. Finally, we add back the corresponding bleaching signal using the obtained overall shape and amplitude. This yields the two-photon $PDF_{\perp}$ shown in Fig. 3E in the main text.

A ridge is defined as a 1-D local maximum in any direction. We use an open-source ImageJ plugin (https://imagej.net/Ridge_Detection) which employs a ridge detection algorithm described by Steger(*42*) to locate all the ridges in the two-photon $PDF_{\perp}$. Once all the ridges are found, a trajectory map can be obtained by simply connecting nearby ridges.

χ^2 Fitting of Transient Structure in One-Photon Channel

To obtain transient molecular structure of the CF_3 group during dissociation, we performed a standard χ^2 fitting procedure on $\Delta PDF_{\perp}$(*37*). The fitting uses two assumptions:

The structure retains the C_{3v} symmetry during dissociation.

The molecular ensemble follows a $\cos^2\theta$ distribution.

C_{3v} symmetry should be maintained during dissociation as long as the rotational distortion timescale is significantly slower than that of the dissociation. Furlan et al (*29*) have concluded that dissociation through A-band excitation of CF_3I is significantly faster than the angular distortion or smearing of the molecule. This conclusion has been widely accepted in previous ion imaging publications (*27*, *43–45*). Point 2 is valid immediately upon dissociation because of the photoselection rule(*41*), but becomes less valid as rotational distortion and dephasing of the CF_3 fragment takes place. This also contributes to the fact that the uncertainty in the fitted results increases after Δt=100 fs. Based on a free-jet expansion model(*46*), the estimated rotational dephasing time for the parent CF_3I is 1.5 ps, and for the CF_3 fragment is roughly 400 fs.

The fitting is performed in 3-D: C-F bond length, F-C-F bond angle, and C-I bond length. These three numbers determine completely the molecular structure under C_{3v} symmetry. Since $\Delta PDF_{\perp}$ is not sensitive to C-I and F-I atom pairs and the iodine is a fast-moving object during dissociation, this fitting only gives reliable results for the C-F bond length and F-C-F bond angle. The fitting starts by simulating diffraction patterns for different molecular geometries, followed by applying the diffraction pattern processing routine to get the $\Delta PDF_{\perp}$, and finally using the simulated $\Delta PDF_{\perp}$ to retrieve the best match. The amplitude is set by the excitation population (5.6%) of the one-photon channel, which is determined separately by the F-I bleaching signal in the $\Delta PDF_{\parallel}$. The range between 1Å and 3Å is used in the fitting, which covers the distance of the C-F pair (1.33 Å), the F-F pair (2.15 Å), and their vibrations. The fitting result is given in Table S1, with the uncertainty representing 95% confidence level. Fig. S5 shows $\Delta PDF_{\perp}$ at two selected times, 20 fs and 87 fs, along with the corresponding best-fits. The ground state C-F bond length and F-C-F bond angle are 1.33 Å and 108.1°, respectively (*47*). Since the vibrational period of both the umbrella and the breathing mode is faster than the instrumental response, the fitting gives an averaged structure over the instrumental response.

Time zero in this experiment is determined by comparing the umbrella opening motion from experiment to simulation, as shown in Fig. 4D.

Ab-initio Multiple Spawning Calculations

For the one-photon channel, we performed Complete Active Space Self Consistent Field (CASSCF) calculations using MOLPRO, with an active space consisting of 6 electrons and 4 orbitals: the two lone-pair p-orbitals on iodine and the C-I σ bonding and anti-bonding orbitals, def2-SVP basis and Stuttgart small core relativistic effective core potential (ECP) on iodine atom. As discussed later in the CF_3I Photoexcitation section, full quantum nuclear dynamics was performed on a three-dimensional fit Hamiltonian incorporating spin-orbit effects, and the results show that different spin-orbit state cannot be observed at the current experimental resolution. Therefore, full-dimensional dynamics simulations are performed using *Ab Initio* Multiple Spawning (AIMS) on electronic states determined without spin-orbit (SO) coupling. Only energy components of the ECPs are used. The influence of SO coupling is primarily limited to a splitting of each state into several states with parallel potential energy surfaces. The averaged structural evolution of $R_{C\text{-}F}$ and ∠FCF is given in Fig. S6.

For the two-photon channel, electronic structure calculations are performed with the Fractional Occupation Molecular Orbital-Complete Active Space Configuration Interaction (FOMO-CASCI) level of theory(*48–50*) using the def2-SVP basis set(*51*) combined with the Stuttgart small core relativistic ECP for Iodine atom, similar to the one-photon channel. A series of 5 even-tempered auxiliary functions with exponents 0.04, 0.02, 0.01, 0.005 and 0.002 bohr^{-2} are added, centered on the iodine atom, to describe the Rydberg states. The active space consists of 6 electrons in 6 orbitals: C-I σ bonding and antibonding orbitals, the two lone-pair p-orbitals on Iodine, and the 6s and 7s Rydberg orbitals. The temperature parameter and occupation scheme in the FOMO-CASCI method was calibrated to reproduce the crossing point between the ion pair and 6s/7s PESs calculated using Multireference Configuration Interaction Singles and Doubles (MRCISD), using the same CAS active space, basis set, and ECP. The calibration is done along a linear dissociation path with the CF_3 group frozen. PES curves at different temperatures are shown in Fig. S7. In general, the shape of the PES exhibits moderate dependency on the FOMO-CASCI fractional occupation temperature over a wide range but exhibits discontinuous behavior when the temperature is too low. Here, as T decreases below 0.12 a.u., discontinuities start to occur around 1.9Å in regions that are relatively high energy but still accessible. As T increases beyond 0.2 a.u., the intersection between the ion pair and 7s states moves to longer bond lengths. This leads to overestimation of simulated lifetimes on 7s and underestimation of the 6s energy and gives rise to crossings between the 6s and valence states at more accessible energies. The best fit to the MRCISD PESs is obtained with T=0.16 a.u., closely reproducing energies of valence and Rydberg states, while only slightly overestimating the energies of the ion pair state. The simulated dataset includes more than 2000 spawned trajectories from 50 initial conditions.

Adiabatic States Assignment

In Fig. 3G in the main text, we show diabatic character (i.e., electronic configuration) of the electronic state for the evolving nuclear wavepacket. In AIMS simulations, each trajectory basis function (TBF) propagates on a specific adiabatic state, which may exhibit different diabatic character at different nuclear configurations. For each time step of each trajectory, we identify the predominant diabatic character of the populated adiabatic state, and the population of the TBF is assigned to this diabatic state. Summation over all initial conditions yields the population profile shown in the figure. In this section, we explain the method for identifying diabatic states.

Because Jahn-Teller distortion is small, the 7s, 6s and valence excited states each form a near-degenerate pair, due to the E electronic symmetry before spin-orbit interactions are included within the C_{3v} point group. Each pair of near-degenerate states is well separated and noncrossing, but they intersect with the nondegenerate ion pair state at different nuclear configurations. In most cases, the energetic spacing of adiabatic states allows for the identification of these near degenerate pairs of states. In the small number of cases where the ion-pair state is energetically close to a degenerate E pair to create three strongly coupled states, we identify the adiabatic state with strongest ion-pair character by inspecting the dipole moment of these three states. To avoid difficulties at the asymptote, we group the ground and valence excited states together to show the total valence state population.

When spin-orbit interactions are included, the Rydberg states further split into different spin-orbit states. However, since the signals from these spin-orbit states are challenging to resolve with the current experimental resolution, we do not include spin-orbit couplings in the simulation. The spin-orbit states are therefore not labeled in Fig. 3G.

Supplementary Text

Complete Experimental Dataset

In the main text, we only show ΔPDF along two specific directions—parallel to laser polarization ($\Delta PDF_{\parallel}$) and perpendicular to laser polarization ($\Delta PDF_{\perp}$). Here we show ΔPDF along 9 different directions in Fig. S8, with each direction averaged within a 10° cone. Examining all directions together, the photoselection rules can be immediately identified—dissociation is a parallel excitation, and non-adiabatic processes are resulted from a perpendicular excitation.

The raw diffraction patterns are averaged over 4 different ranges of time delays, after a median filter and a normalization to the total diffraction signal, are shown in Fig. S9.

Separating One-Photon and Two-Photon Signal in $\Delta PDF_{\perp}$

In the main text we use timescale to roughly separate the one-photon and two-photon signal in $\Delta PDF_{\perp}$, with Δt>200 fs dominated by the two-photon channel and Δt<200 fs dominated by the one-photon channel. This is because the dissociation and vibration immediately start around time zero, which gives a sudden strong change in $PDF_{\perp}$. This signal dominates over the two-photon signal, because the one-photon channel has roughly 4 times larger population than the two-photon channel. Between Δt=200 fs and Δt=600 fs, the one-photon induced dissociation is complete and the vibrational modes are relatively steady, and they do not cause any change in $PDF_{\perp}$ except a smooth decay caused by rotational dephasing. Therefore, in this time window the nonadiabatic dynamics from the two-photon channel prevails.

Here we use AIMS simulation results to support this argument. Fig. S10A shows the simulated $\Delta PDF_{\perp}$ for one-photon channel. The difference signal starts around time zero, where two bleaching pair distances (2 Å and 2.9 Å) and three increasing pair distances (1.5 Å, 2.4 Å, and 3.5 Å) can be identified. The two bleaching features are the loss of original F-F and F-I distances, the positive feature at 1.5 Å is the signature of C-F stretching vibration, the positive feature at 2.4 Å is the signature of umbrella vibration, and the positive feature at 3.5 Å is the dissociating portion of the wavepacket. Except for the fast-traveling dissociating wavepacket, these features can be identified in the experimental $\Delta PDF_{\perp}$ (Fig. 3A in the main text).

After ~200 fs, the simulated $\Delta PDF_{\perp}$ in Fig. S10A starts to decay smoothly for all the pair distances between 1 and 2.6 Å, and remains constant for pair distances larger than 2.6 Å. This is due to rotational dephasing of the vibrationally hot CF_3 fragment. Because the CF_3 fragment is very hot vibrationally, the C-F and F-F atom pair distances distribute over almost all distances between 1 and 2.6 Å. In a CF_3 fragment, the C-F and F-F atom pairs are originally born preferentially in the perpendicular direction due to the photoselection rules. Once rotationally dephased, they will be distributed in all directions nearly uniformly, resulting in a net loss in $\Delta PDF_{\perp}$. This is the origin of the monotonic decay between 1 and 2.6 Å. The parent CF_3I will also rotationally dephase, but on a much longer timescale, because CF_3 has a significantly smaller moment of inertia compare to CF_3I. The estimated $1/e$ rotational dephasing timescale is 400 fs for CF_3 and 1.5 ps for CF_3I.

Because of the monotonicity of the one-photon signal after Δt=200 fs, any oscillatory signal seen in $\Delta PDF_{\perp}$ after Δt=200fs must come from the two-photon channel. Fig. S10B shows the $\Delta PDF_{\perp}$ for the two-photon channel and Fig. S10C shows the combined $\Delta PDF_{\perp}$ from both channels, with a one-photon-to-two-photon branching ratio of 80:20. This figure shows that before ~200fs, the features are mostly dominated by the one-photon channel and after ~200fs the features are mostly dominated by the two-photon channel.

The simulated $\Delta PDF_{\parallel}$ for the one-photon channel, two-photon channel and the combination of both channels are given in Fig. S10D-F. These figures show that the $\Delta PDF_{\parallel}$ signal is dominated by the one-photon channel.

Two-Photon Excitation Ambiguity

At our pump wavelength 264.5 nm, the two-photon energy is centered at 9.37 eV. Sutcliffe and Walsh have measured a 132.3 nm absorption band in CF_3I in their pioneering work in 1960, and tentatively assigned it to the Rydberg [5pπ^3, $^2\Pi_{1/2}$](7s) state(*52*). This assignment has been adopted by many following works (*25*, *30*–*32*).

In 2006, Eden and co-workers have reported a high resolution VUV absorption spectrum in CF_3I(*35*). They identified two nearby series, the $v_{0\text{-}0}$ band of one series located at 9.46 eV and the other located at 9.55 eV. The series starting at 9.37 eV is identified as the $v_{2\text{-}0}$ vibrational transition of the 9.46 eV series. They have assigned the 9.46 eV series as the Rydberg [5pπ^3, $^2\Pi_{3/2}$](8s) state and the 9.55 eV series as the Rydberg [5pπ^3, $^2\Pi_{1/2}$](7s) state. This proposed assignment has quite high uncertainty. The assignment is based on Rydberg formula together with previously measured ionization potential (IP) (*53*). Using the IP listed in NIST Chemistry Webbook (IP=10.28 ± 0.07 eV) (*54*), 9.46 eV corresponds to the Rydberg [5pπ^3, $^2\Pi_{3/2}$](8s) state; while using IP measured by Macleod (IP=10.37 eV) (*55*), 9.46 eV corresponds to the Rydberg [5pπ^3, $^2\Pi_{1/2}$](7s) state. For this reason, it is uncertain that which of the two states our two-photon channel was excited to.

Because the two states are so close in energy, the ambiguity has not yet been resolved with existing experimental technique and is beyond the scope of this work. In this manuscript, we follow the assignment of Rydberg [$5p\pi^3$, $^2\Pi_{1/2}$](7s) state, but we note that we cannot exclude that the final state of the two-photon excitation might be the Rydberg [$5p\pi^3$, $^2\Pi_{3/2}$](8s) state.

The dynamics on the Rydberg [$5p\pi^3$, $^2\Pi_{3/2}$](8s) surface and Rydberg [$5p\pi^3$, $^2\Pi_{1/2}$](7s) surface are similar, because they are almost parallel to each other, close in energy, and both strongly couple to the ion-pair state. We performed AIMS simulation on the 8s state, and the simulated $\Delta PDF_{\perp}$ is shown in Fig. S11. This simulation shows similar dynamics as shown on the 7s surface in Fig. 3C, with small differences in vibrational magnitude and recurrence time. This shows that even if the final state of the two-photon excitation is indeed Rydberg [$5p\pi^3$, $^2\Pi_{3/2}$](8s), the main conclusions of this manuscript do not change.

CF_3I Photoexcitation

The one-photon excitation and ensuing dissociation process of CF_3I has long been considered as a prototype for understanding photodissociation and curve-crossing processes. As a result, a large number of theoretical and experimental studies are available, and it is well-known that there are three possible transitions: a strong parallel transition to $^3Q_0^+$ state, and weaker perpendicular transitions to $^1Q_1$ and $^3Q_1$ states. The transition to the triplet-dominant $^3Q_0^+$ state is made possible by the strong spin-orbit effect of iodine atom, causing the $\tilde{X}$ state to carry a small triplet component, and the $^3Q_0^+$ state to contain a small singlet contribution. The $\tilde{X}$ and $^3Q_0^+$ states are both of A_1 symmetry, and the direction of the transition dipole is parallel to the C3 symmetry axis.

In order to verify our theoretical setup, we took the Spin Orbit matrix elements, including the potential energy surfaces, and constructed analytical quasi-diabatic Hamiltonians within a three dimensional subspace containing the one-dimensional C-I dissociation, CF_3 umbrella motion and the bending of I atom relative to the CF_3 fragment, which is kept symmetric and C-F distance frozen at Frank-Condon geometry, using the same coordinate system and kinetic energy operator as in previous work on CH_3I (*56*). Then we conducted numerically exact quantum dynamics using MCTDH (*20*) with this 3-D model, and computed the absorption spectrum by Fourier transformation of the autocorrelation function. The relative transition dipole moments to $^3Q_{0+}$ and $^1Q_1$ states are taken from Van Veen *et al*(*57*). The electronic structure calculations used to fit the model are performed at the CASSCF level using a 6 electron 4 orbital active space including the C-I σ and σ* orbitals and the degenerate p_x and p_y lone pair orbitals iodine, with def2-SVP basis set and Stuttgart relativistic ECP on Iodine atom. The PES with SO splitting and the absorption spectrum are shown in Fig. S12. The $^3Q_0^+$ state is dominant in absorption cross section in A band, whereas the absorption spectrum for the $^1Q_1$ state is overall weaker, and almost exactly vanishing at the laser energy of the experimental measurements. This is confirmed by many previous experimental studies(*27*, *29*, *44*, *58*). The simulated absorption spectrum matches very well with the magnetic circular dichroism measurement by Gedanken (*58*).

Compared to the one-photon process, the two-photon excitation to [$5p\pi^3$, $^2\Pi_{1/2}$](7s) Rydberg state is less studied, and critical information such as the cross-section, intermediate states and photoselection rules have not been elucidated. Nevertheless, this channel was observed in multiple previous experiments. Rydberg s states split into two sets of spin-orbit states that correspond to the $E_{1/2}$ and $E_{3/2}$ states of the CF_3I^+ cation. Each set further splits into predominantly singlet and triplet states. These states can be denoted with the same Mulliken symbols. Among these spin-orbit states, the transition to $^3Q_0^+(7s)$ is allowed through two parallel excitations, whereas transitions to all 7s spin-orbit states through two perpendicular excitations are allowed, because E×E spans all irreducible representations in C_{3v} point group.

The PESs of the Rydberg states are nearly identical to the corresponding ionic states, therefore all Rydberg states concerned here are nearly parallel, with very weak couplings to other states and long lifetimes. The quasi-stable nature of the Rydberg states serves to significantly strengthen their absorption cross sections. This is manifested in the fact that the one-photon photoexcitation cross sections to the Rydberg states are around 100 times stronger than that to the $^3Q_{0+}$ valence excitation. This accounts for the observed signal from two-photon excitation.

Multiphoton Ionization

In this experiment, photoionization channels corresponding to an excitation process of three and more photons are possible. In this section, we will discuss the possible signatures of these channels, and give an upper estimate of how much these ionization channels can contribute to the two-photon signal we observe.

The three-photon energy would be 14.09 eV, enough to populate both the $\tilde{A}$ cation state (13.25 eV) and $\tilde{X}$ cation state (10.45 eV) of CF_3I^+(*59*). Previous literature suggests that $\tilde{X}$ is a bound state and $\tilde{A}$ is a dissociative state(*44*, *60*). In order to understand the dynamics in this excitation channel on femtosecond timescale, we simulated the dynamics of these two states.

For the $\tilde{A}$ state, we calculated the gradient descent path on the CF_3I^+ $\tilde{A}$ state potential energy surfaces starting from the Frank Condon point (see Fig. S13). There is no barrier from the FC geometry to the asymptote, and the PES is strongly repulsive. Fast dissociation similar to the one-photon excitation process is therefore expected. For this reason, the dynamics of this channel is likely to closely track the one-photon dissociation signal and cannot explain the 200fs C-I stretching vibration or the recurrence signal at 500fs in the perpendicular direction.

For the $\tilde{X}$ state, we have simulated the C-I bond stretching dynamics using full quantum wave packet simulation on a one-dimensional model, with the CF_3 moiety frozen and only the I atom moving along the symmetry axis. At this geometry, the pair of E states of the $\tilde{X}$ state are exactly degenerate, and therefore is treated as a single state and the dynamic simulation is fully adiabatic. The energies are performed from CASSCF calculations and a (5, 5) active space, with TZVP basis. The C-I bond vibrates with a ~160fs period. The nuclear wavepacket dynamics is shown in Fig. S14. This channel might contribute to the ~200fs C-I stretching signal we observe but will not contribute to the recurrence at 3Å/500fs.

Here we show a direct experimental measurement of ionization population, using an additional dataset that is taken under higher laser intensity. This result helps us to establish an upper limit of the cation signal.

The most obvious electron diffraction signature of ionization is that the unscreened positive charge in the molecular ion will result in a sharply rising diffraction intensity as $s \rightarrow 0$, since the Rutherford scattering has an apparent singularity for small angle elastic scattering(*61*). Such signature can be used to measure the absolute quantity of the ion. This phenomenon, however, requires access to $s < 1$ Å^{-1}, while the dataset presented in the original manuscript can only access $s > 1.2$ Å^{-1}.

We have taken another dataset (not used in the original manuscript) that allows us to access down to $s = 0.52$ Å^{-1}, as shown in Fig. S15. For convenience, we will name the original dataset as dataset 1 and this new dataset as dataset 2. Dataset 2 is taken at roughly 20% higher laser intensity, but with only 10% integration time per delay point as compare to dataset 1. In addition, dataset 2 only goes up to a time delay of 400fs. Nevertheless, since the Rutherford scattering scales as s^{-4}, the ion scattering signal at low s is very strong and more than enough to give reliable measurement of ionization population.

The same data analysis process is applied to dataset 2 and the results are given in Fig. S16. In comparison to dataset 1 (Fig. 3A and Fig. 4A in the main text), similar features can be identified, but the PDF maps are in general noisier because of that the total amount of data per delay point is only 10%. The one-photon dissociation population is determined to be 12% (dataset 1 is 5.6%). The absolute excitation percentage depends on the overlap between laser, electron and molecular beams and varies from dataset to dataset. For this reason, we compare excitation population of different channels by normalizing to the one-photon channel. The excitation ratio for the one-photon, two-photon and three-photon has a linear, quadratic and cubic dependence on laser power. Therefore, after normalizing to the one-photon excitation ratio, the power dependence is linear for a two-photon process and quadratic for a three-photon process.

The change in the raw diffraction pattern of dataset 2, after a radial average, is given in Fig. S17A. It is very obvious that there is an increase in low s. Fig. S17B gives the average diffraction-difference signal between 300 and 400 fs. A sharp rise can be seen in s between 0.5 and 1 Å^{-1}, while the simulated C-I dissociation (red curve) should have led to a negative signal. This positive signal is a direct diffraction signature of ionization.

The diffraction signature from neutral molecules and ions can be simulated with a simple model(*61*, *62*):

$$f_{neutral}(\theta) = \frac{8\pi^2 me^2}{h^2}\frac{Z - F(\theta)}{s^2}$$

$$f_{ion}(\theta) = f_{neutral}(\theta) + \frac{8\pi^2 me^2}{h^2}\frac{\Delta Z}{s^2} \quad (5)$$

where m is electron mass, e is elementary charge, h is Planck constant, Z is atomic number, s is momentum change, F is identical with the atomic scattering factor of x-rays, and ΔZ is the ionic charge. Z and F represent scattering from the nucleus and electron cloud, respectively. At $\theta = 0$, $F(\theta)=Z$, and the scattering amplitude goes to zero, indicating the nuclear charge is screened by electrons in neutral molecules. For ions, the ΔZ term represents the divergent scattering amplitude from the unscreened Coulomb potential. We use the equation above to calculate the total atomic scattering cross section for CF_3I and CF_3I^+. The results are given in Fig. S17C. The ionic scattering becomes roughly 4.8 times higher than the neutral CF_3I at $s = 0.53$ Å^{-1}.

In dataset 2, assuming the sharp increase at $s = 0.53$ Å^{-1} is coming from singly charged CF_3I^+, the required ion population would be 1.17±0.18%. This is roughly 10% of the population of the one-photon channel. Note that any dynamics with a charge separation character, such as the ion-pair state involved in the two-photon channel, will give rise to a dipole and can also lead to divergent scattering as $s \rightarrow 0$(*63*). Therefore, this analysis gives an upper limit for the ionization population.

The worst-case scenario corresponds to the following assumptions:

1. All the low-*s* signal comes from ionization (ignoring all dipole contributions).
2. All the ionization population goes to the $\tilde{X}$ cation state.
3. All the ionization results in perpendicular signals.
4. Rydberg states are fully ionized, resulting in a quadratic power dependence of absolute excitation ratio, and linear excitation ratio relative to the one-photon process.

These assumptions yield a $\tilde{X}$ cation state population of 8% (in comparison to the one-photon channel) in dataset 1. The two-photon population is roughly 25% of the single photon channel. Therefore, the $\tilde{X}$ cation state contributes less than a third of the C-I stretching vibration in $\Delta PDF_\perp$, and assumption 4 is clearly incorrect.

Since most neutral two-photon products are not ionized, the ionization therefore should assume a third-order dependency on laser power. We can now relax condition 4 to assume that the relative excitation ratio with respect to the one-photon process is quadratic. This instead yields an upper bound for cation $\tilde{X}$ state population of 6% relative to the one-photon process, and ionization should contribute less than one quarter of the vibrational signals observed in $\Delta PDF_\perp$. Since conditions 1-3 all result in some degree of overestimation of the ionic contribution, the actual contribution from ionization in the in $\Delta PDF_\perp$ can be significantly lower.

For multiphoton processes with four or more photons, the cross-section will be even lower, and the molecule is more likely to promptly dissociate because of the extremely high energy put into the molecule. We therefore conclude that although additional multiphoton excitation channels are possible they contribute no more than a quarter of the C-I stretching vibration in $\Delta PDF_\perp$, and they will not contribute to the recurrence signal at 3Å/500fs.

Generality of the Method

The experimental and data analysis method described in this report is generally applicable to small polyatomic molecules in the gas phase. Currently, the major experimental constraints are:

- Vapor pressure. A number density on the order of 10^{16}cm^{-3} is required to achieve a reasonable diffraction signal.

- Time scale of the dynamical process. The current temporal resolution is limited to ~150 fs, although better temporal resolution can be expected in the near future.
- Time window for the anisotropy analysis. The anisotropy will be lost once the rotational dephasing takes place. This gives a window of measurement for the anisotropy analysis. For this experiment, the CF_3 fragment and CF_3I molecule have a dephasing timescale of roughly 400 fs and 1.5 ps, respectively. For molecules with smaller moment of inertia, the window will be smaller.

The atomic scattering cross-section roughly scales as Z^2, where Z is the atom number. This indicates that lighter atoms will have weaker signal. This work has demonstrated that the motion of light elements, such as carbon and fluorine, can be resolved. For hydrogen, it is challenging to resolve with the current signal level. For a molecule like CH_3I, the C-I atom pair will be roughly 5 times brighter than H-I atom pairs, and at least 20 times brighter than the rest of the atom pairs. Therefore, it allows one to focus on the C-I bond dynamics, and the analysis will be much more simplified.

Because of the fact that the atom pair signal is proportional to the product of the atomic scattering cross section of the two atoms, heavy scattering element such as iodine can be used to amplify weak scattering signals.

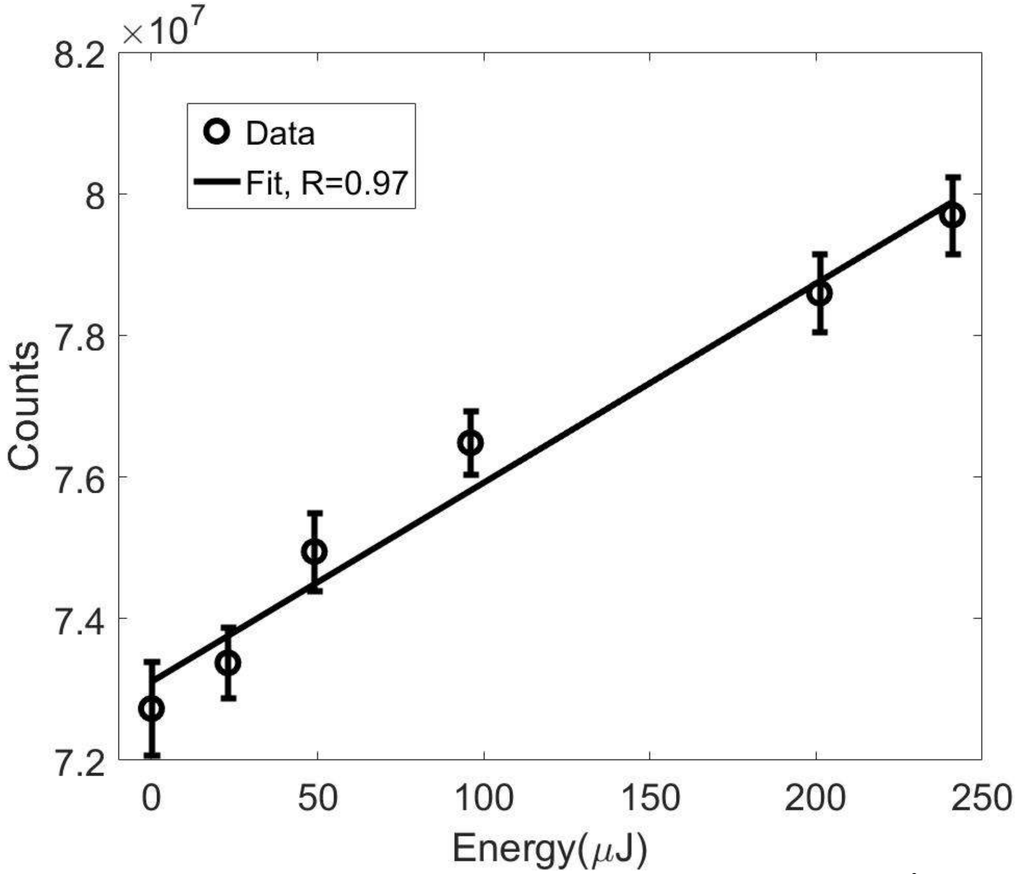

Fig. S1. Pump fluence scan. The total counts in the region between 1.6 Å^{-1} and 2.3 Å^{-1} at Δt = 600 fs as a function of pump pulse energy. All data shown in the main text are taken at a pump pulse energy of 200 μJ.

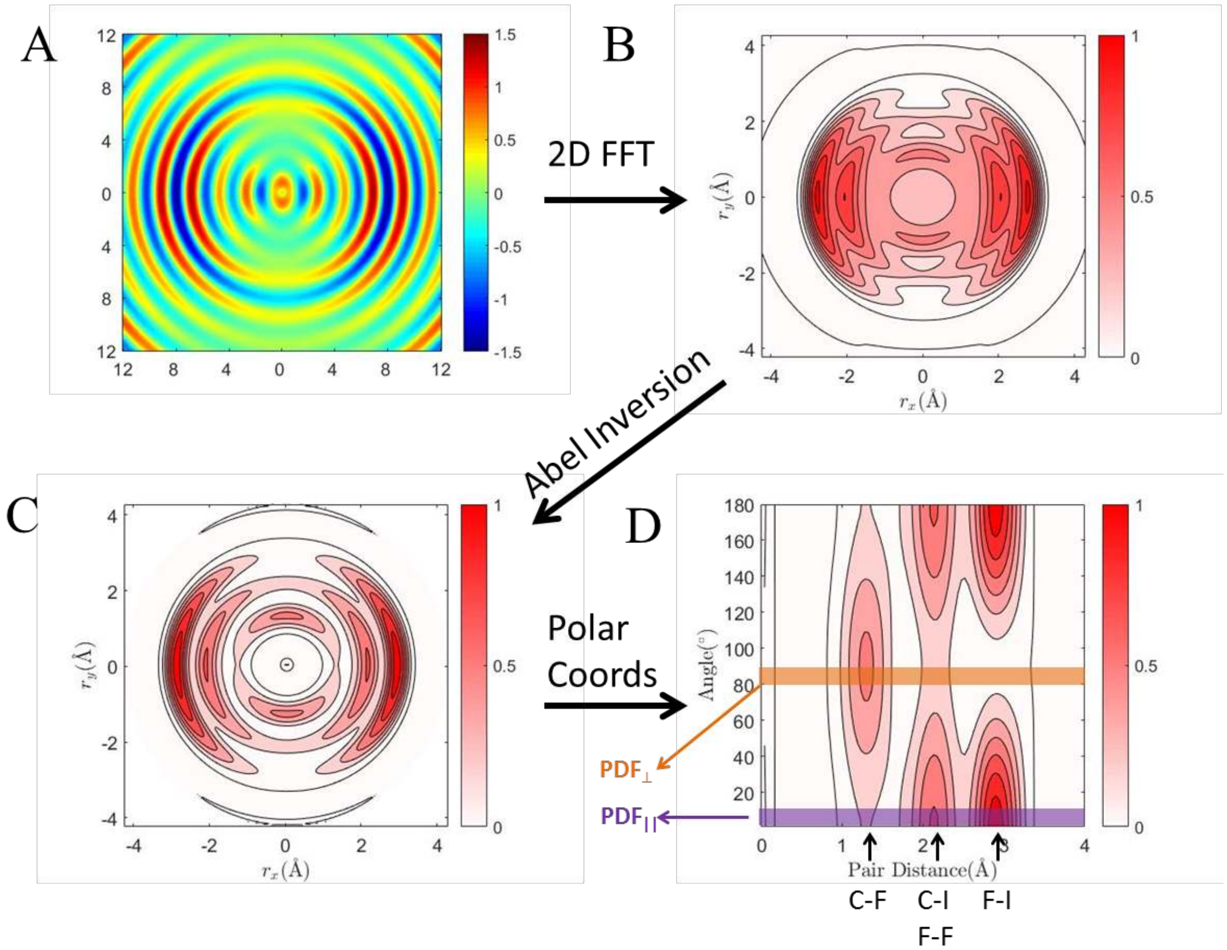

Fig. S2. Graphic illustration for diffraction pattern analysis procedure. (A) Simulated diffraction pattern for ground state CF_3I with a $\cos^2\theta$ distribution. (B) Projected PDF obtained by a 2-D FFT of part (A). (C) 2-D slice of PDF obtained by an Abel inversion of part (B). (D) Same PDF as part (C) but shown in polar coordinates. Each peak corresponds to an atom pair, marked in the bottom. Area covered by purple and brown strips are $PDF_{\parallel}$ (0°-10°) and $PDF_{\perp}$ (80°-90°), respectively.

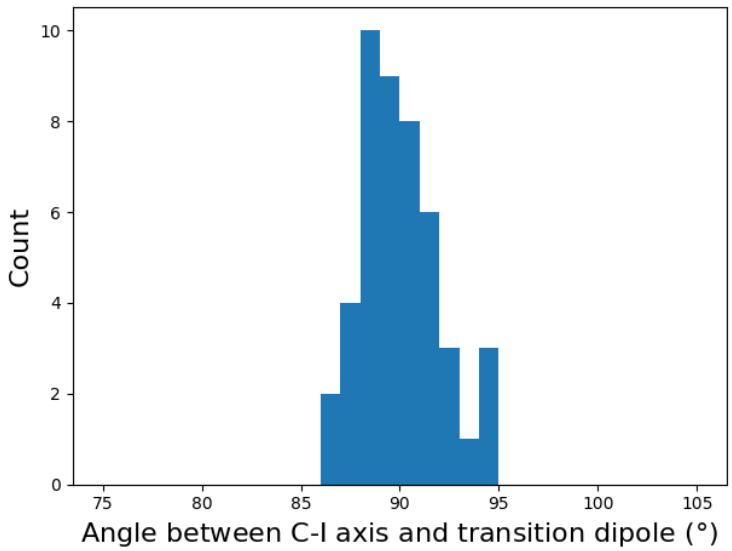

Fig S3. Angle between the C-I axis and the ground → Rydberg 7s transition dipole.

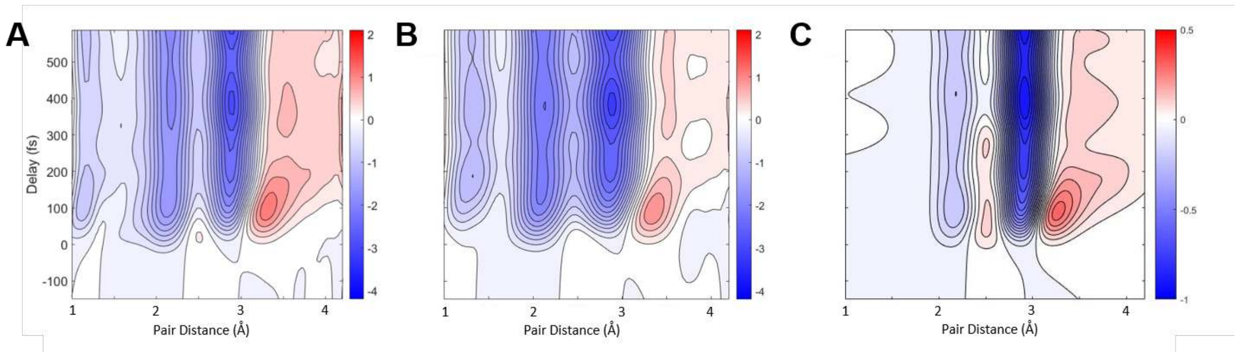

Fig. S4 Simulated ΔPDF$_\perp$ using different methods. Starting from the same trajectories, these three patterns are simulated using different methods described in the "Validity of the Fourier Analysis" section. The vertical axes of all three figures are identical.

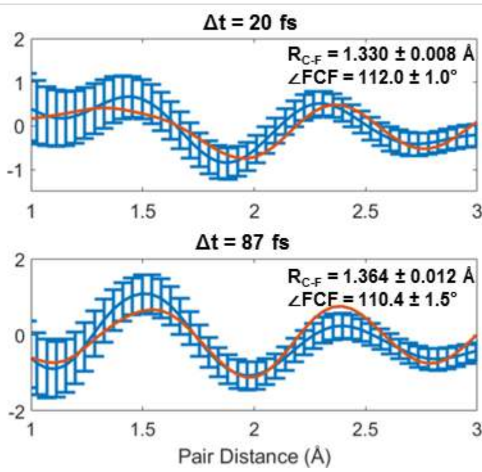

Fig. S5. Chi-square structure fit of experimental ΔPDF$_\perp$ at 20 fs and 87 fs.

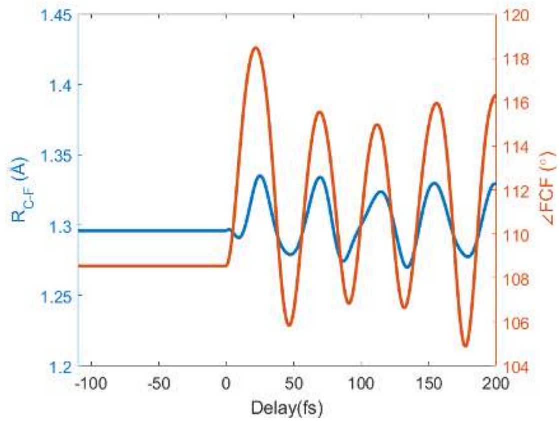

Fig. S6. Simulated structural evolution after one-photon excitation. $R_{C\text{-}F}$ and ∠FCF are color-coded as blue and red, respectively. The vertical axes range for length and angle are adjusted to match each other with a 1.33Å (ground state C-F distance) radius.

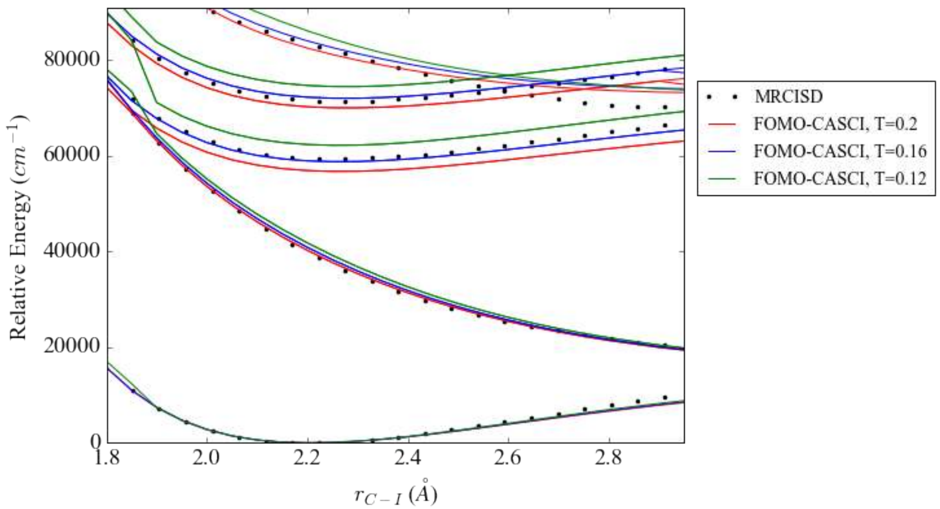

Fig. S7. Calibration of the Temperature Parameter in FOMO-CASCI. Blue curve shows the FOMO-CASCI PES at optimal temperature of 0.16 atomic units, while red and green curves correspond to slightly lower and higher temperatures.

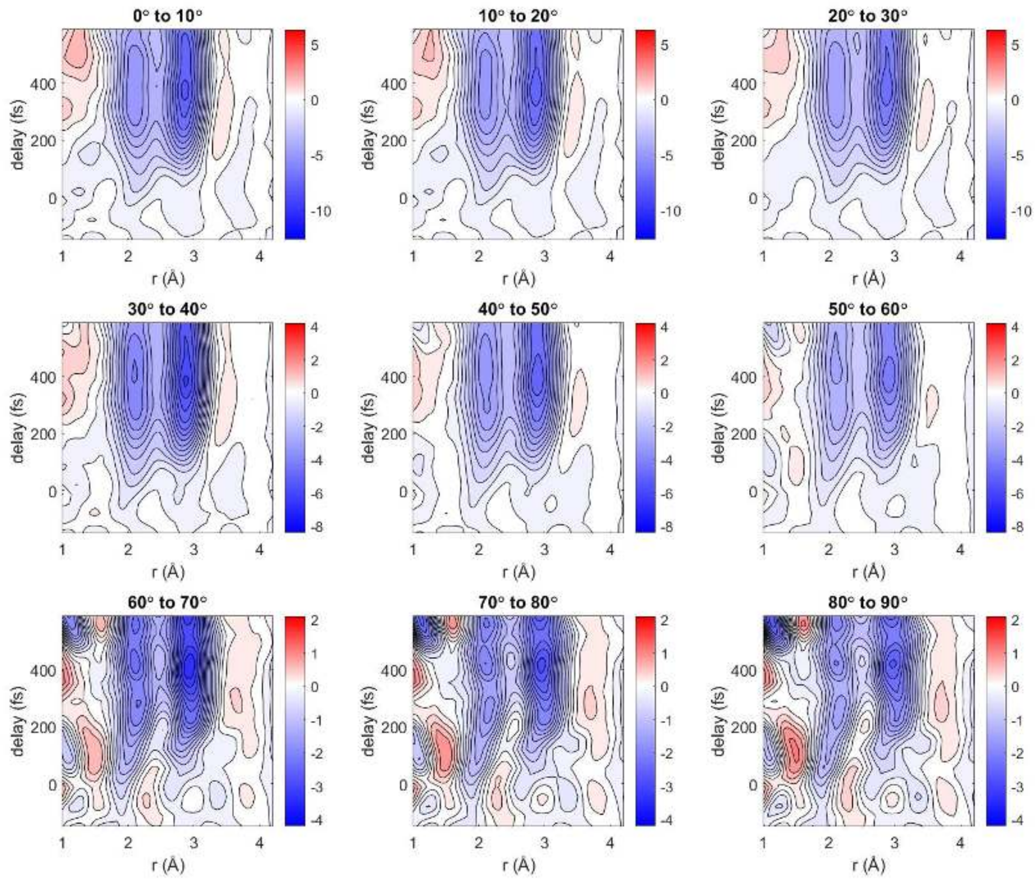

Fig. S8. Complete experimental dataset. Each panel shows the ΔPDF within a 10° cone. Angle is measured with respect to the laser polarization. Note that the color scale of each row is different. The middle row is twice the scale of the bottom row and top row is three times the scale of the bottom row.

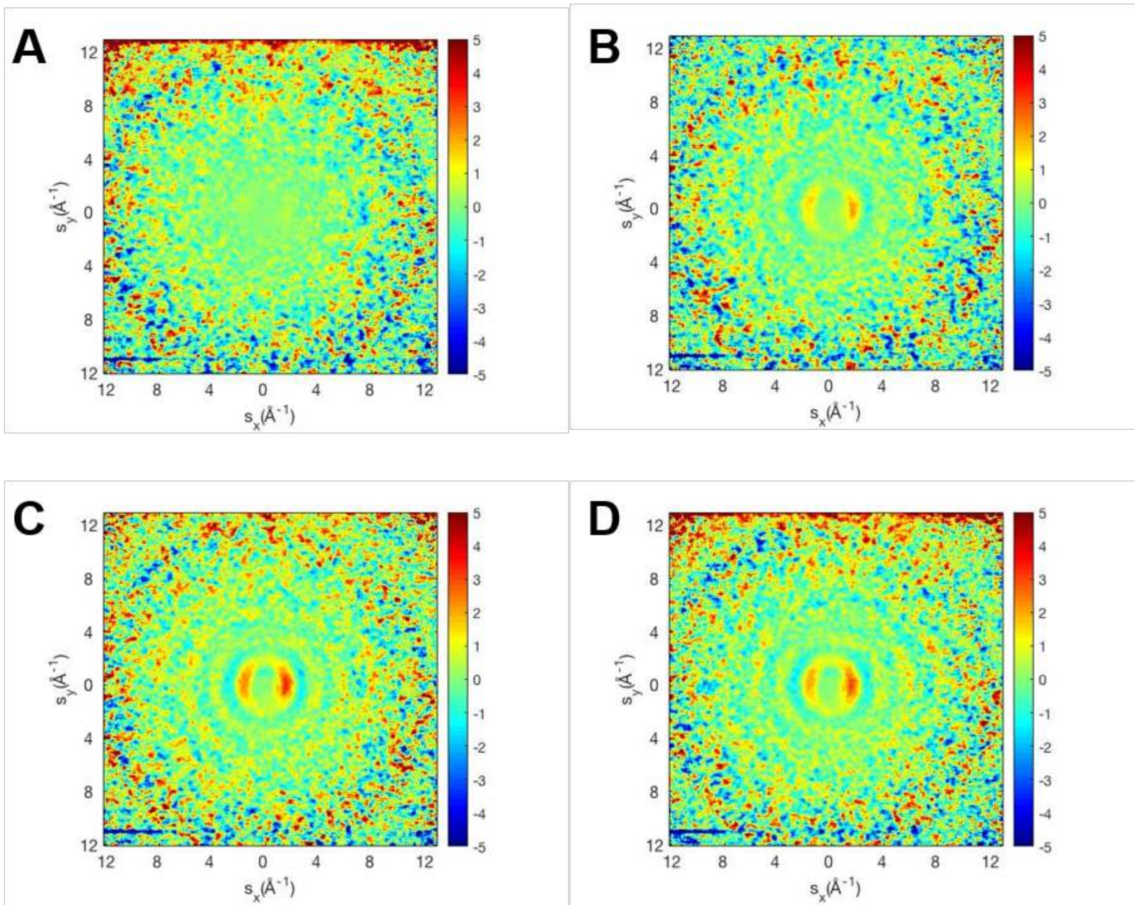

Fig. S9. Experimental Diffraction Patterns. Raw diffraction patterns after a median filter, averaged between delay time of (A) -50 fs and 90 fs, (B) 120 fs and 260 fs, (C) 290 fs and 430 fs, (D) 450 fs and 590 fs. Each pattern contains roughly 6 hours of data.

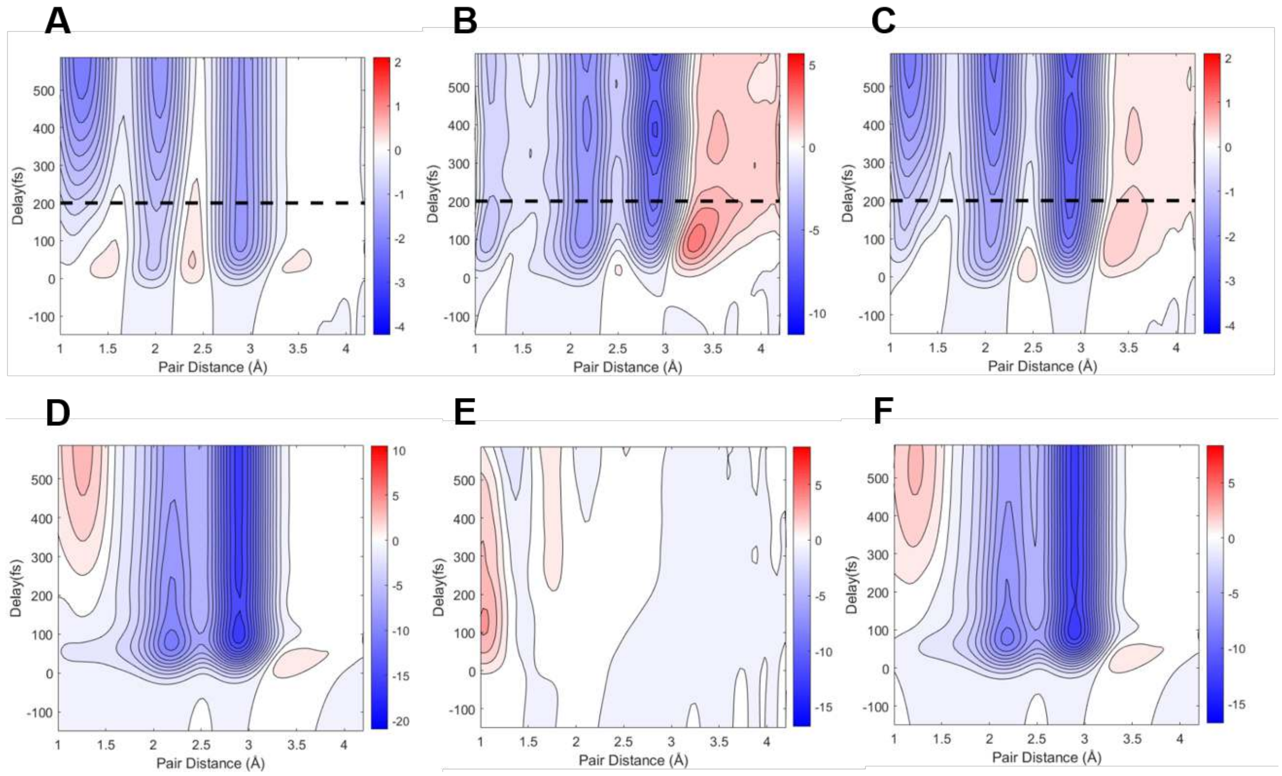

Fig. S10. Simulated ΔPDF using AIMS. (A) Simulated $\Delta PDF_{\perp}$ for one-photon channel. (B) Simulated $\Delta PDF_{\perp}$ for two-photon channel. (C) Simulated $\Delta PDF_{\perp}$ for both one-photon and two-photon channels, with a one-photon-to-two-photon branching ratio of 80:20. (D) Simulated $\Delta PDF_{\parallel}$ for one-photon channel. (E) Simulated $\Delta PDF_{\parallel}$ for two-photon channel. (F) Simulated $\Delta PDF_{\parallel}$ for both one-photon and two-photon channels, with a one-photon-to-two-photon branching ratio of 80:20. The dashed line at 200fs in parts (A)-(C) indicates a rough separation between the signal from the one-photon and the two-photon channel.

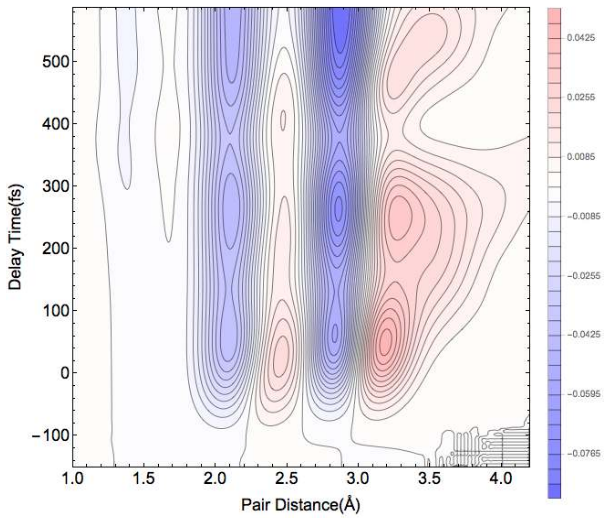

Fig. S11. Simulated ΔPDF$_\perp$ on Rydberg [5pπ^3, $^2\Pi_{3/2}$](8s) state.

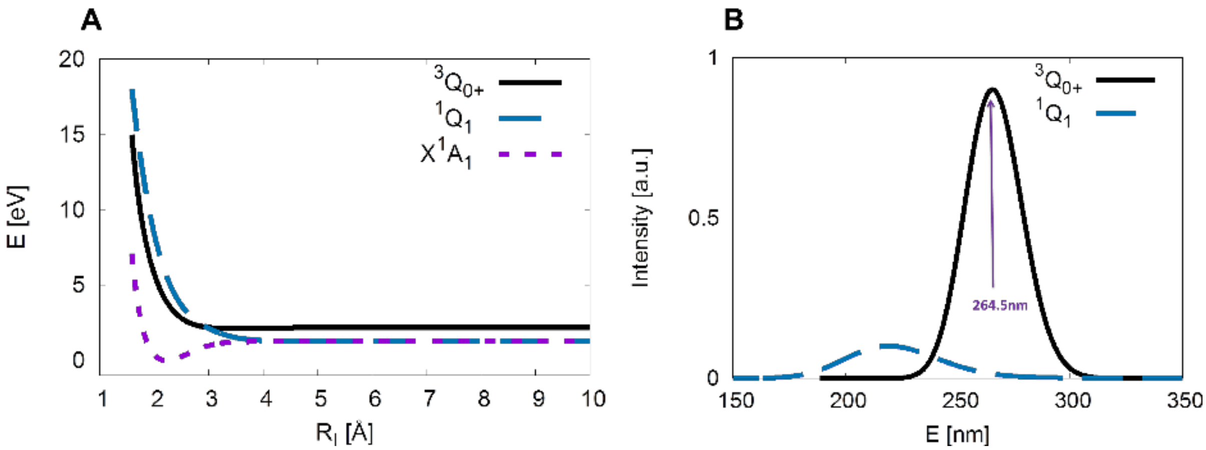

Fig. S12. Verification of CASSCF method, basis set and ECP. (A) One-dimensional coupled PESs along C-I coordinate at CASSCF level including SO effects, and (B) absorption spectrum computed using the autocorrelation function obtained from full-quantum dynamics on the model PESs. Experimental excitation wavelength is marked by the purple arrow.

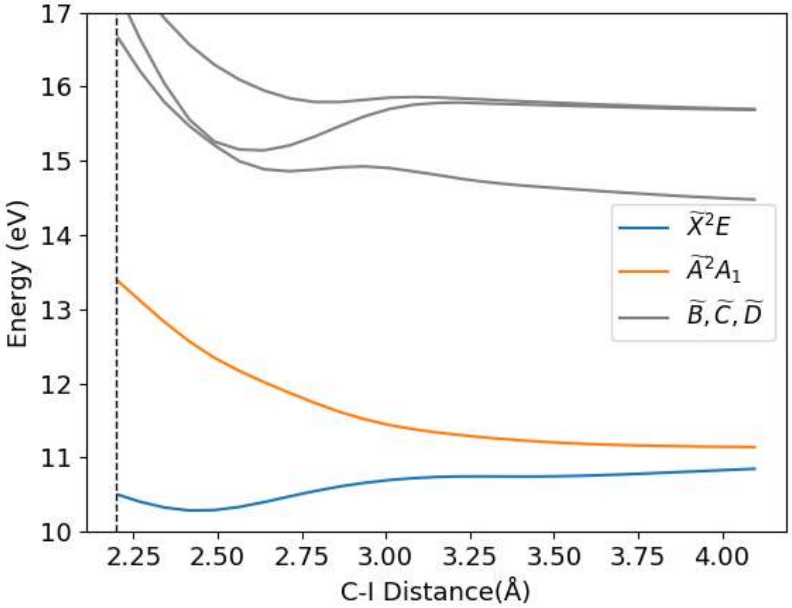

Figure S13. **Potential energy surfaces of CF_3I^+ ionic states.** PESs are plotted along the gradient descent path on the $\tilde{A}^2A_1$ state starting from the Frank-Condon point. The C-I distance corresponding to the FC point is labeled with vertical dashed line. The PESs are calculated at MRCISD level. Energies are relative to the global minimum of neutral CF_3I.

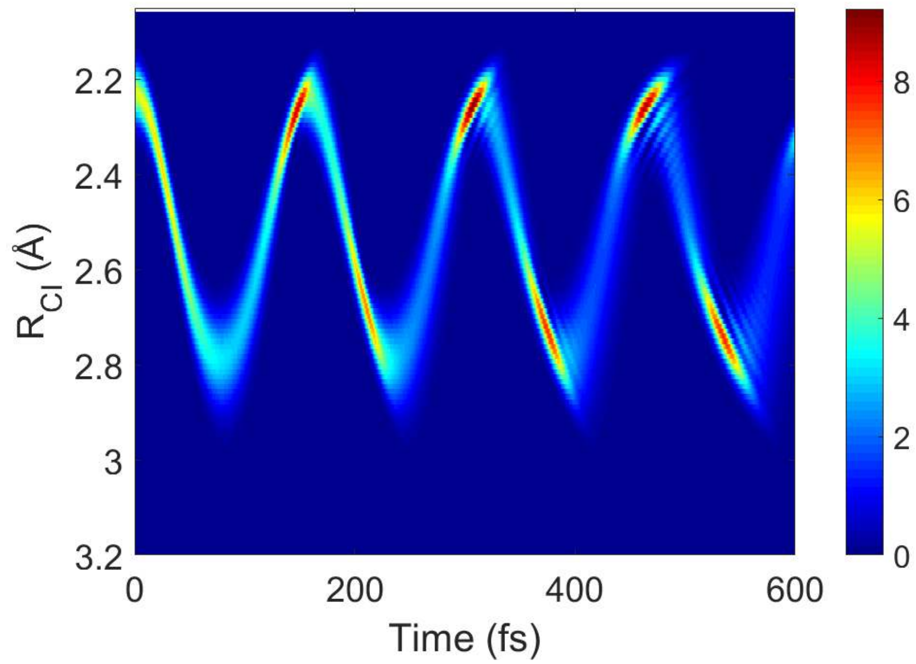

Figure S14. Simulated wavepacket dynamics of CF_3I^+ on $\tilde{X}$ cation state using full quantum wave packet simulation on the 1-dimensional model.

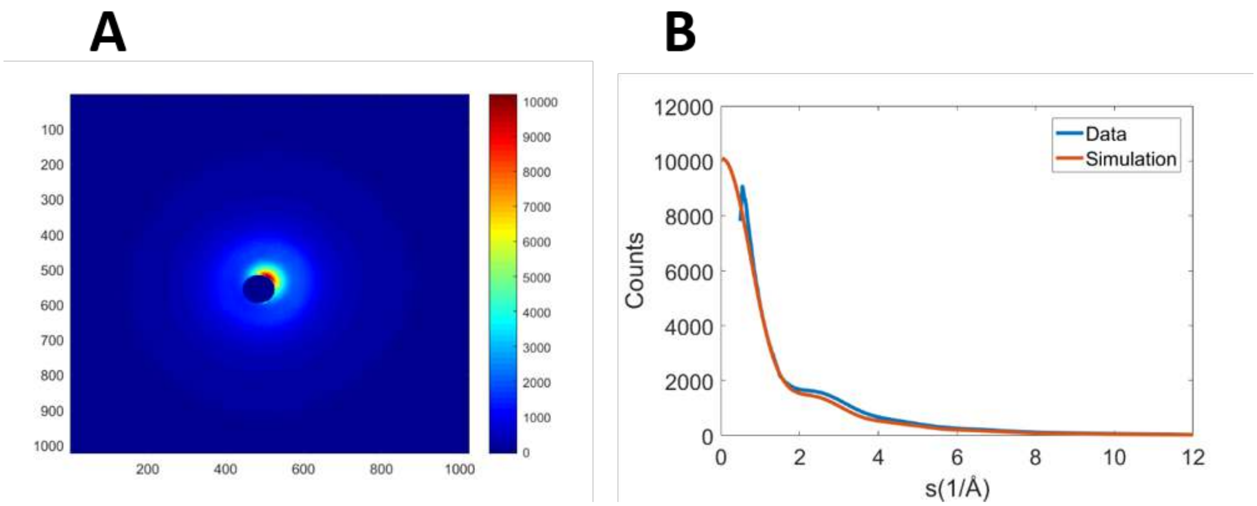

Figure S15. Diffraction pattern with low-*s* access. A. Raw diffraction pattern of CF_3I; low-*s* is accessed by shifting the diffraction pattern off-center. B. Radial average of diffraction pattern shows that reliable diffraction signal goes down to s = 0.52 Å^{-1}.

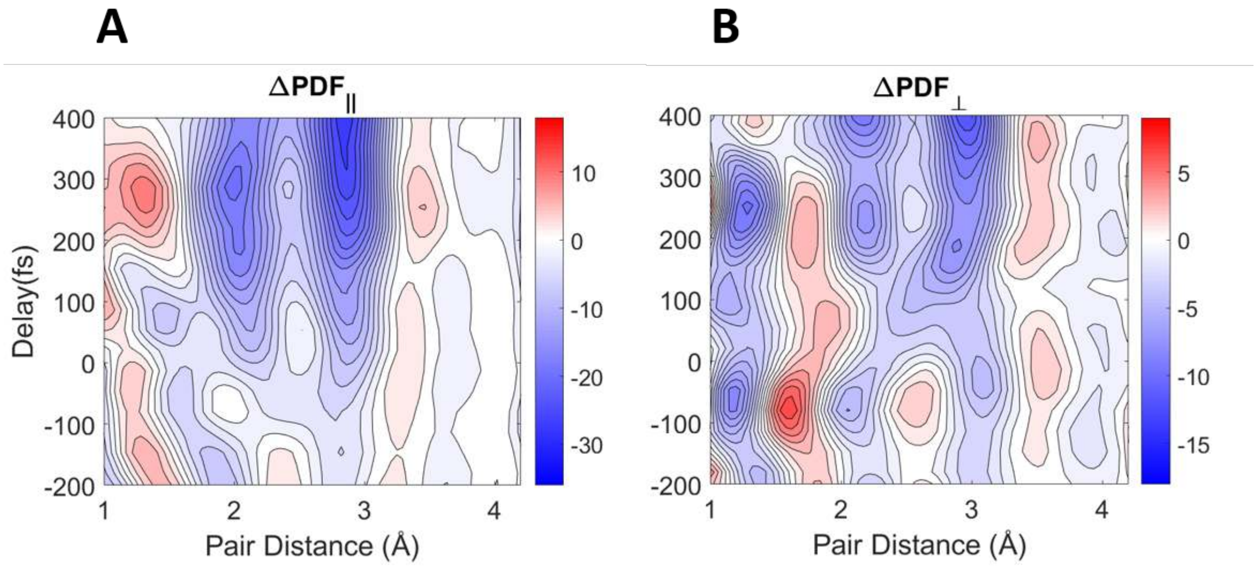

Figure S16. Pair distribution function change of dataset 2 in parallel (A) and perpendicular (B) directions.

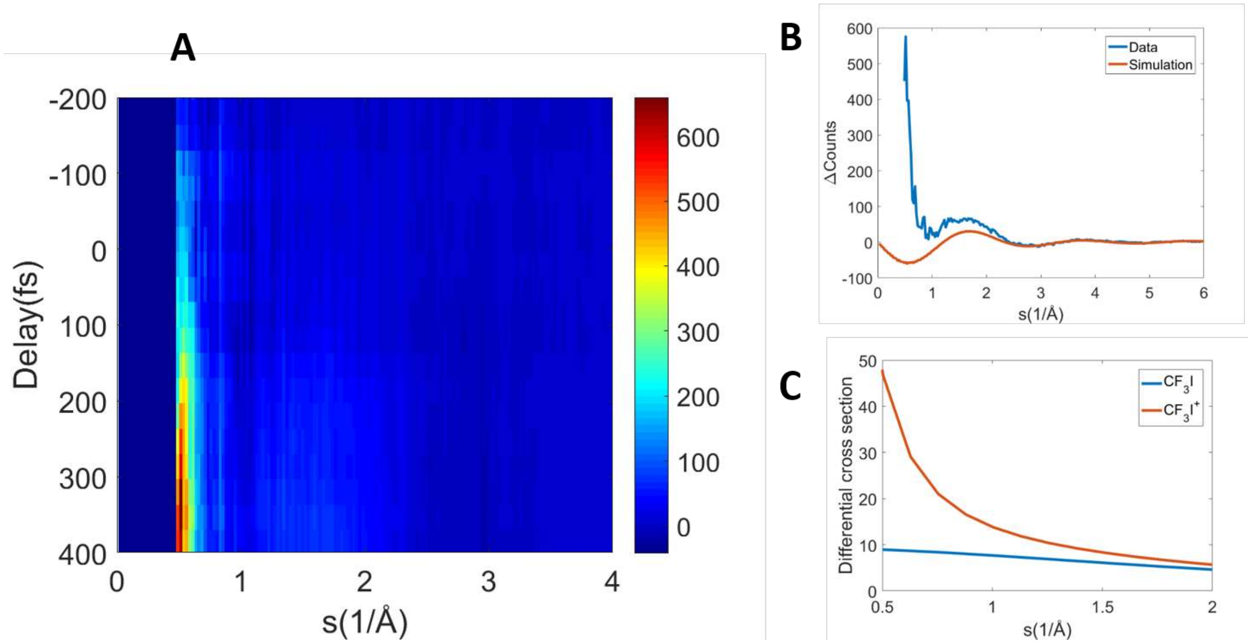

Figure S17. Electron diffraction signature of ionization. A. Change in raw diffraction as a function of delay time. B. Change in raw diffraction between time delay of 300 fs and 400 fs (blue), and simulated diffraction signal for C-I dissociation (red). C. Simulated elastic scattering cross section for neutral CF_3I and CF_3I^+ cation.

Table S1 – Measured structural change in CF_3 group during dissociation

Time Delay (fs)	C-F bond length (Å)	F-C-F bond angle (°)
-80	1.344±0.007	107.8±0.9
-47	1.334±0.011	109.2±1.4
-13	1.322±0.010	111.0±1.2
20	1.330±0.008	112.0±1.0
53	1.354±0.010	111.4±1.2
87	1.364±0.012	110.4±1.5
120	1.360±0.015	110.4±1.9
153	1.358±0.018	111.2±2.3
187	1.352±0.023	111.6±2.8
220	1.336±0.025	111.4±3.2

Movie S1

This movie shows the structural response of CF_3 group during dissociation, and is made with data shown in Table S1, or Fig. 4D in the main text. The motion is presented in the rest frame of the carbon atom. The left-hand side gives a ball-and-stick model of the molecule, and the right-hand side shows a zoom-in view of the trajectory of one of the fluorine atoms. C-F bond length and F-C-F bond angle are displayed in the bottom right.

References and Notes

1. G. Herzberg, *Molecular Spectra and Molecular Structure III (Polyatomic Molecules)* (1966).

2. J. Michl, V. Bonacic-Koutecky, *Electronic Aspects of Organic Photochemistry* (Wiley, 1990).

3. W. Domcke, D. R. Yarkony, H. Köppel, *Conical Intersections—Electronic Structure, Dynamics and Spectroscopy* (World Scientific Pub, 2004).

4. Y.-C. Cheng, G. R. Fleming, Dynamics of light harvesting in photosynthesis. *Annu. Rev. Phys. Chem.* **60**, 241–262 (2009). doi:10.1146/annurev.physchem.040808.090259 Medline

5. D. Polli, P. Altoè, O. Weingart, K. M. Spillane, C. Manzoni, D. Brida, G. Tomasello, G. Orlandi, P. Kukura, R. A. Mathies, M. Garavelli, G. Cerullo, Conical intersection dynamics of the primary photoisomerization event in vision. *Nature* **467**, 440–443 (2010). doi:10.1038/nature09346 Medline

6. C. E. Crespo-Hernández, B. Cohen, P. M. Hare, B. Kohler, Ultrafast excited-state dynamics in nucleic acids. *Chem. Rev.* **104**, 1977–2019 (2004). doi:10.1021/cr0206770 Medline

7. M. F. Holick, Photosynthesis of vitamin D in the skin: Effect of environmental and life-style variables. *Fed. Proc.* **46**, 1876–1882 (1987). Medline

8. J. S. Lim, S. K. Kim, Experimental probing of conical intersection dynamics in the photodissociation of thioanisole. *Nat. Chem.* **2**, 627–632 (2010). doi:10.1038/nchem.702 Medline

9. J. A. DeVine, M. L. Weichman, B. Laws, J. Chang, M. C. Babin, G. Balerdi, C. Xie, C. L. Malbon, W. C. Lineberger, D. R. Yarkony, R. W. Field, S. T. Gibson, J. Ma, H. Guo, D. M. Neumark, Encoding of vinylidene isomerization in its anion photoelectron spectrum. *Science* **358**, 336–339 (2017). doi:10.1126/science.aao1905 Medline

10. H. J. Wörner, J. B. Bertrand, B. Fabre, J. Higuet, H. Ruf, A. Dubrouil, S. Patchkovskii, M. Spanner, Y. Mairesse, V. Blanchet, E. Mével, E. Constant, P. B. Corkum, D. M. Villeneuve, Conical intersection dynamics in NO_2 probed by homodyne high-harmonic spectroscopy. *Science* **334**, 208–212 (2011). doi:10.1126/science.1208664 Medline

11. A. Stolow, A. E. Bragg, D. M. Neumark, Femtosecond time-resolved photoelectron spectroscopy. *Chem. Rev.* **104**, 1719–1757 (2004). doi:10.1021/cr020683w Medline

12. J. Brazard, L. A. Bizimana, T. Gellen, W. P. Carbery, D. B. Turner, Experimental Detection of Branching at a Conical Intersection in a Highly Fluorescent Molecule. *J. Phys. Chem. Lett.* **7**, 14–19 (2016). doi:10.1021/acs.jpclett.5b02476 Medline

13. T. J. A. Wolf, R. H. Myhre, J. P. Cryan, S. Coriani, R. J. Squibb, A. Battistoni, N. Berrah, C. Bostedt, P. Bucksbaum, G. Coslovich, R. Feifel, K. J. Gaffney, J. Grilj, T. J. Martinez, S. Miyabe, S. P. Moeller, M. Mucke, A. Natan, R. Obaid, T. Osipov, O. Plekan, S. Wang, H. Koch, M. Gühr, Probing ultrafast ππ*/nπ* internal conversion in organic chromophores via K-edge resonant absorption. *Nat. Commun.* **8**, 29 (2017). doi:10.1038/s41467-017-00069-7 Medline

14. A. H. Zewail, Femtochemistry: Atomic-scale dynamics of the chemical bond using ultrafast lasers (Nobel Lecture). *Angew. Chem. Int. Ed.* **39**, 2586–2631 (2000). doi:10.1002/1521-3773(20000804)39:15<2586:AID-ANIE2586>3.0.CO;2-O Medline

15. M. P. Minitti, J. M. Budarz, A. Kirrander, J. S. Robinson, D. Ratner, T. J. Lane, D. Zhu, J. M. Glownia, M. Kozina, H. T. Lemke, M. Sikorski, Y. Feng, S. Nelson, K. Saita, B. Stankus, T. Northey, J. B. Hastings, P. M. Weber, Imaging Molecular Motion: Femtosecond X-Ray Scattering of an Electrocyclic Chemical Reaction. *Phys. Rev. Lett.* **114**, 255501 (2015). doi:10.1103/PhysRevLett.114.255501 Medline

16. J. Küpper, S. Stern, L. Holmegaard, F. Filsinger, A. Rouzée, A. Rudenko, P. Johnsson, A. V. Martin, M. Adolph, A. Aquila, S. Bajt, A. Barty, C. Bostedt, J. Bozek, C. Caleman, R. Coffee, N. Coppola, T. Delmas, S. Epp, B. Erk, L. Foucar, T. Gorkhover, L. Gumprecht, A. Hartmann, R. Hartmann, G. Hauser, P. Holl, A. Hömke, N. Kimmel, F. Krasniqi, K.-U. Kühnel, J. Maurer, M. Messerschmidt, R. Moshammer, C. Reich, B. Rudek, R. Santra, I. Schlichting, C. Schmidt, S. Schorb, J. Schulz, H. Soltau, J. C. H. Spence, D. Starodub, L. Strüder, J. Thøgersen, M. J. J. Vrakking, G. Weidenspointner, T. A. White, C. Wunderer, G. Meijer, J. Ullrich, H. Stapelfeldt, D. Rolles, H. N. Chapman, X-ray diffraction from isolated and strongly aligned gas-phase molecules with a free-electron laser. *Phys. Rev. Lett.* **112**, 083002 (2014). doi:10.1103/PhysRevLett.112.083002

17. J. Yang, M. Guehr, X. Shen, R. Li, T. Vecchione, R. Coffee, J. Corbett, A. Fry, N. Hartmann, C. Hast, K. Hegazy, K. Jobe, I. Makasyuk, J. Robinson, M. S. Robinson, S. Vetter, S. Weathersby, C. Yoneda, X. Wang, M. Centurion, Diffractive Imaging of Coherent Nuclear Motion in Isolated Molecules. *Phys. Rev. Lett.* **117**, 153002 (2016). doi:10.1103/PhysRevLett.117.153002 Medline

18. A. A. Ischenko, P. M. Weber, R. J. D. Miller, Capturing chemistry in action with electrons: Realization of atomically resolved reaction dynamics. *Chem. Rev.* **117**, 11066–11124 (2017). doi:10.1021/acs.chemrev.6b00770 Medline

19. R. Chen, H. Guo, Evolution of quantum system in order domain of Chebyshev operator. *J. Chem. Phys.* **105**, 3569–3578 (1996). doi:10.1063/1.472228

20. H.-D. Meyer, U. Manthe, L. S. Cederbaum, The multi-configurational time-dependent Hartree approach. *Chem. Phys. Lett.* **165**, 73–78 (1990). doi:10.1016/0009-2614(90)87014-I

21. J. C. Tully, Molecular dynamics with electronic transitions. *J. Chem. Phys.* **93**, 1061–1071 (1990). doi:10.1063/1.459170

22. H.-D. Meyer, W. H. Miller, A classical analog for electronic degrees of freedom in nonadiabatic collision processes. *J. Chem. Phys.* **70**, 3214–3223 (1979). doi:10.1063/1.437910

23. M. Ben-Nun, J. Quenneville, T. J. Martínez, Ab initio multiple spawning: Photochemistry from first principles quantum molecular dynamics. *J. Phys. Chem. A* **104**, 5161–5175 (2000). doi:10.1021/jp994174i

24. The square bracket encloses the electronic configuration, symmetry, and spin-orbit state of the cation core, and the parenthesis indicates the configuration of the Rydberg electron.

25. S. Yin, H. P. Liu, J. Y. Zhang, B. Jiang, L. Wang, G. H. Sha, N. Q. Lou, Femtosecond pump–probe mass spectra on the dissociative photoionization of CF3I. *Chem. Phys. Lett.* **372**, 904–910 (2003). doi:10.1016/S0009-2614(03)00555-4

26. L. J. Butler, Chemical reaction dynamics beyond the Born-Oppenheimer approximation. *Annu. Rev. Phys. Chem.* **49**, 125–171 (1998). doi:10.1146/annurev.physchem.49.1.125 Medline

27. F. Aguirre, S. T. Pratt, Photoionization of vibrationally hot CH_3 and CF_3. *J. Chem. Phys.* **122**, 234303 (2005). doi:10.1063/1.1931507 Medline

28. M. Zahedi, J. Harrison, J. W. Nibler, 266 nm CH_3I photodissociation: CH_3 spectra and population distributions by coherent Raman spectroscopy. *J. Chem. Phys.* **100**, 4043–4055 (1994). doi:10.1063/1.466342

29. A. Furlan, T. Gejo, J. R. Huber, Probing curve crossing by wavelength-dependent recoil anisotropy : The photodissociation of CF 3 I at 275–303 nm studied by photofragment translational spectroscopy. *J. Phys. Chem.* **100**, 7956–7961 (1996). doi:10.1021/jp953130g

30. H. P. Liu, Z. G. Sun, S. D. Hogan, N. Q. Lou, Photodissociation dynamics of CF_3I investigated by two-color femtosecond laser pulses. *Eur. Phys. J. D* **40**, 357–362 (2006). doi:10.1140/epjd/e2006-00183-2

31. W. G. Roeterdink, M. H. M. Janssen, Femtosecond velocity map imaging of dissociative ionization dynamics in CF3I. *Phys. Chem. Chem. Phys.* **4**, 601–612 (2002). doi:10.1039/b107897f

32. W. G. Roeterdink, M. H. M. Janssen, Velocity map imaging of femtosecond photodynamics in CF3I. *Chem. Phys. Lett.* **345**, 72–80 (2001). doi:10.1016/S0009-2614(01)00865-X

33. J. Yang, M. Guehr, T. Vecchione, M. S. Robinson, R. Li, N. Hartmann, X. Shen, R. Coffee, J. Corbett, A. Fry, K. Gaffney, T. Gorkhover, C. Hast, K. Jobe, I. Makasyuk, A. Reid, J. Robinson, S. Vetter, F. Wang, S. Weathersby, C. Yoneda, M. Centurion, X. Wang, Diffractive imaging of a rotational wavepacket in nitrogen molecules with femtosecond megaelectronvolt electron pulses. *Nat. Commun.* **7**, 11232 (2016). doi:10.1038/ncomms11232 Medline

34. S. P. Weathersby, G. Brown, M. Centurion, T. F. Chase, R. Coffee, J. Corbett, J. P. Eichner, J. C. Frisch, A. R. Fry, M. Gühr, N. Hartmann, C. Hast, R. Hettel, R. K. Jobe, E. N. Jongewaard, J. R. Lewandowski, R. K. Li, A. M. Lindenberg, I. Makasyuk, J. E. May, D. McCormick, M. N. Nguyen, A. H. Reid, X. Shen, K. Sokolowski-Tinten, T. Vecchione, S. L. Vetter, J. Wu, J. Yang, H. A. Dürr, X. J. Wang, Mega-electron-volt ultrafast electron diffraction at SLAC National Accelerator Laboratory. *Rev. Sci. Instrum.* **86**, 073702 (2015). doi:10.1063/1.4926994 Medline

35. S. Eden, P. Limão-Vieira, S. V. Hoffmann, N. J. Mason, VUV photoabsorption in CF3X (X = Cl, Br, I) fluoro-alkanes. *Chem. Phys.* **323**, 313–333 (2006). doi:10.1016/j.chemphys.2005.09.040

36. J. Yang *et al.*, Imaging CF3I conical intersection and photodissociation dynamics by ultrafast electron diffraction. Figshare (2018); doi:10.6084/m9.figshare.6169427.

37. R. Srinivasan, V. A. Lobastov, C.-Y. Ruan, A. H. Zewail, Ultrafast electron diffraction (UED): A new development for the 4D determination of transient molecular structures. *Helv. Chim. Acta* **86**, 1761–1838 (2003). doi:10.1002/hlca.200390147

38. J. S. Baskin, A. H. Zewail, Ultrafast electron diffraction: Oriented molecular structures in space and time. *ChemPhysChem* **6**, 2261–2276 (2005). doi:10.1002/cphc.200500331 Medline

39. G. Garcia, L. Nahon, I. Powis, Two-dimensional charged particle image inversion using a polar basis function expansion. *Rev. Sci. Instrum.* **75**, 4989–4996 (2004). doi:10.1063/1.1807578

40. J. M. Glownia, A. Natan, J. P. Cryan, R. Hartsock, M. Kozina, M. P. Minitti, S. Nelson, J. Robinson, T. Sato, T. van Driel, G. Welch, C. Weninger, D. Zhu, P. H. Bucksbaum, Self-referenced coherent diffraction x-ray movie of Ångstrom- and femtosecond-scale atomic motion. *Phys. Rev. Lett.* **117**, 153003 (2016). doi:10.1103/PhysRevLett.117.153003 Medline

41. R. N. Zare, *Angular Momentum* (Wiley, New York, 1988).

42. G. Steger, An unbiased detector of curvilinear structures. *IEEE Trans. Pattern Anal. Mach. Intell.* **20**, 113–125 (1998). doi:10.1109/34.659930

43. F. Aguirre, S. T. Pratt, Velocity map imaging of the photodissociation of CF3I: Vibrational energy dependence of the recoil anisotropy. *J. Chem. Phys.* **118**, 1175–1183 (2003). doi:10.1063/1.1530582

44. F. Aguirre, S. T. Pratt, Velocity map imaging of the photodissociation of CF3I+ in the Ã←X̃ band. *J. Chem. Phys.* **119**, 9476–9485 (2003). doi:10.1063/1.1615523

45. P. Felder, Photodissociation of CF3I at 248 nm: Kinetic energy dependence of the recoil anisotropy. *Chem. Phys.* **155**, 435–445 (1991). doi:10.1016/0301-0104(91)80119-3

46. O. F. Hagena, Nucleation and growth of clusters in expanding nozzle flows. *Surf. Sci. Lett.* **106**, 101–116 (1981). doi:10.1016/0039-6028(81)90187-4

47. V. Typke, M. Dakkouri, H. Onerhammer, On the molecular structure of X-CF3 molecules (X = Cl, Br, I). *J. Mol. Struct.* **44**, 85–96 (1978). doi:10.1016/0022-2860(78)85008-X

48. P. Slavícek, T. J. Martínez, Ab initio floating occupation molecular orbital-complete active space configuration interaction: An efficient approximation to CASSCF. *J. Chem. Phys.* **132**, 234102 (2010). doi:10.1063/1.3436501 Medline

49. E. G. Hohenstein, M. E. F. Bouduban, C. Song, N. Luehr, I. S. Ufimtsev, T. J. Martínez, Analytic first derivatives of floating occupation molecular orbital-complete active space configuration interaction on graphical processing units. *J. Chem. Phys.* **143**, 014111 (2015). doi:10.1063/1.4923259 Medline

50. E. G. Hohenstein, Analytic formulation of derivative coupling vectors for complete active space configuration interaction wavefunctions with floating occupation molecular orbitals. *J. Chem. Phys.* **145**, 174110 (2016). doi:10.1063/1.4966235 Medline

51. F. Weigend, R. Ahlrichs, Balanced basis sets of split valence, triple zeta valence and quadruple zeta valence quality for H to Rn: Design and assessment of accuracy. *Phys. Chem. Chem. Phys.* **7**, 3297–3305 (2005). doi:10.1039/b508541a Medline

52. L. H. Sutcliffe, A. D. Walsh, Far ultra-violet absorption spectrum of trifluoro methyl iodide. *Trans. Faraday Soc.* **57**, 873–883 (1961). doi:10.1039/tf9615700873

53. S. Eden, thesis, University College London (2003).

54. P. J. Linstrom, W. G. Mallard, *NIST Chemistry webBook, NIST Standard Reference Database Number 69* (2014); http://webbook.nist.gov/chemistry.

55. N. A. Macleod, S. Wang, J. Hennessy, T. Ridley, K. P. Lawley, R. J. Donovan, Ionic and Rydberg states of CF_3I studied by high resolution photoelectron (ZEKE-PFI) and resonance-enhanced multiphoton ionisation spectroscopy. *J. Chem. Soc. Faraday Trans.* **94**, 2689–2694 (1998). doi:10.1039/a803515f

56. H. Guo, Three-dimensional photodissociation dynamics of methyl iodide. *J. Chem. Phys.* **96**, 6629–6642 (1992). doi:10.1063/1.462602

57. G. N. A. Van Veen, T. Baller, A. E. De Vries, Photofragmentation of CF_3I in the A band. *Chem. Phys.* **93**, 277–291 (1985). doi:10.1016/0301-0104(85)80025-2

58. A. Gedanken, The magnetic circular dichroism of the A band in CF_3I, C_2H_5I and t-BuI. *Chem. Phys. Lett.* **137**, 462–466 (1987). doi:10.1016/0009-2614(87)80234-8

59. B. W. Yates, K. H. Tan, G. M. Bancroft, J. S. Tse, A variable energy photoelectron study of the valence levels and I 4d core levels of CF_3I. *J. Chem. Phys.* **85**, 3840–3850 (1986). doi:10.1063/1.450904

60. F. Aguirre, S. T. Pratt, Ion-imaging of the photodissociation of CF_3I^+. *J. Chem. Phys.* **118**, 6318–6326 (2003). doi:10.1063/1.1559679

61. L. M. Peng, Electron scattering factors of ions and their parameterization. *Acta Crystallogr. A* **54**, 481–485 (1998). doi:10.1107/S0108767398001901

62. L. O. Brockway, Electron diffraction by gas molecules. *Rev. Mod. Phys.* **8**, 231–266 (1936). doi:10.1103/RevModPhys.8.231

63. P. B. Burt, W. E. Gettys, H. W. Graben, Electron scattering from real dipoles. *Phys. Lett.* **29**, 261–262 (1969). doi:10.1016/0375-9601(69)90371-5